Materials Transactions, Vol. 67, No. 4 (2026) pp. 385 to 404
©2026 The Japan Institute of Metals and Materials

OVERVIEW

Phenomenology and Mechanisms of Hydrogen–Induced Solid Solution–Hardening in Fe–Cr–Ni Austenitic Steels*[1]

Yuhei Ogawa[1,*2], Osamu Takakuwa[2], Junichiro Moriyama[3], Haruki Nishida[1,4,*3], Kaneaki Tsuzaki[1,2] and Akinobu Shibata[1,4]

[1]*Research Center for Structural Materials, National Institute for Materials Science (NIMS), Tsukuba 305-0047, Japan*
[2]*Department of Mechanical Engineering, Kyushu University, Fukuoka 819-0395, Japan*
[3]*Department of Mechanical Systems Engineering, Shinshu University, Nagano 380-8553, Japan*
[4]*NIMS Joint Subprogram in Materials Science and Engineering, Degree Programs in Pure and Applied Sciences, Graduate School of Science and Technology, University of Tsukuba, Tsukuba 305-8577, Japan*

As for the alloying additions of carbon (C) and nitrogen (N), the involvement of solute hydrogen (H) in face–centered–cubic (FCC) Fe–Cr–Ni–based austenitic steels causes considerable magnitude of solid solution–hardening. Notably, the strengthening ability of these three interstitial elements is almost comparable to each other, although H is significantly smaller than C and N in its atomic size. The present paper overviews the phenomenology of such H–induced solid solution–hardening and its underlying rationales in commercial 300–series Fe–Cr–Ni austenitic steels after uniform H–charging in pressurized gaseous H_2 environment at elevated temperatures. The effects of H concentration, deformation temperature, strain rate, and chemical composition of the alloy, as well as the thermal activation process of deformation, are extensively reviewed based mainly on the authors' recent works. Potential roles of three key factors: 1) *solute drag* of H atmosphere around a dislocation; 2) *H–diffusion–controlled glide* of dislocation core; and 3) the presence of *H–substitutional complex*, are discussed in light of the conventionally established theories of dislocation dynamics and plasticity. The H–induced solid solution–hardening is maximized when the factors 1) and 2) (*i.e.*, dynamic interactions between diffusible H and mobile dislocation) exert primary contributions to the flow stress. This fact is attributed to the exclusively high mobility of H atoms in austenite lattice even at around an ambient temperature, which is not the case for C and N that remain immobile during the deformation. [doi:10.2320/matertrans.MT-M2025161]

(Received December 1, 2025; Accepted January 6, 2026; Published January 23, 2026)

Keywords: *austenitic steels, strengthening, interstitial atoms, hydrogen*

1. Introduction

Hydrogen, a potential energy carrier for achieving carbon neutrality, has attracted increasing attention from global society—especially since the 2000s—as a solution to worsening environmental issues and the depletion of fossil fuels. However, for structural metallic materials that are used for long durations under severe hydrogenating conditions in hydrogen–utilizing equipment, concerns on hydrogen embrittlement (*i.e.*, degradation of strength, ductility, and other mechanical properties due to the ingress of hydrogen atoms) [1, 2] remain an unresolved technical issue. In hydrogen refueling stations for fuel cell vehicles—representative hydrogen–utilizing facilities—components such as pipes, joints, valves, and dispenser nozzles, which come into contact with high–pressure hydrogen (H_2) gas, are made of 300–series austenitic stainless steels primarily composed of Fe–Cr–Ni. Austenitic steels with a face–centered–cubic (FCC) crystal structure may also suffer embrittlement through stress– or strain–induced phase transformation to body–centered–cubic (BCC) or hexagonal–close–packed (HCP) structures during plastic deformation. However, when FCC matrix remains stable throughout deformation, these steels exhibit superior resistance to hydrogen embrittlement compared to other steel types [3–8]. Accordingly, in currently operating hydrogen refueling stations, materials such as JIS–SUS316 and SUS316L—classified as stable austenitic steels—are mainly employed. Suitable materials are selected under strict regulations regarding the total threshold amount of Ni and other FCC–stabilizing elements (*i.e.*, Ni equivalent) [9, 10].

Despite their excellent resistance to hydrogen embrittlement, the yield strength of stable austenitic steels at room temperature is generally limited to 200–300 MPa. Their strength is significantly lower than the yield strength of medium carbon steels or low–alloy steels (400–800 MPa), which are widely used in structural applications, thereby leading to a reduction in allowable stress and an increase in material thickness. Solid solution–hardening through the addition of carbon (C) and nitrogen (N) [11–15], dispersion–hardening *via* precipitation of γ′ ($Ni_3(Al,Ti)$) phases or carbides such as VC [16, 17], and grain refinement [18, 19] have long been studied as effective strengthening methods for austenitic steels. Among them, solid solution–hardening can be combined additively with all other strengthening mechanisms [20], making it the most fundamental approach. Hydrogen (H), one of the interstitial elements, typically induces solid solution–hardening in FCC materials similar to other elements, while it is commonly accompanied by a trade–off in degraded ductility [8, 21, 22]. However, the present authors recently discovered that when high concentrations of H are added to specific types of stable austenitic steels—such as SUS310S (Type310S) and SUS309S (Type309S)—both yield and tensile strength increase proportionally with H concentration, without compromising the intrinsic ductility of the material [23–25]. Notably, the increase in yield strength due to H is comparable to that achieved by the same atomic concentration of C or N (Fig. 1).

*[1]This Paper was Originally Published in Japanese in J. Japan Inst. Met. Mater. **89** (2025) 287–306.
*[2]Corresponding author, E-mail: OGAWA.Yuhei@nims.go.jp
*[3]Graduate Student, University of Tsukuba

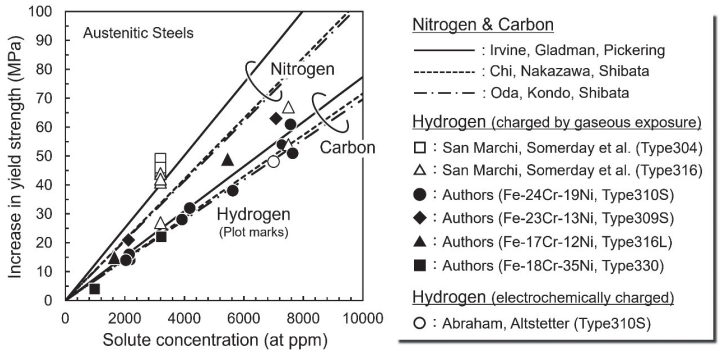

Fig. 1 Solid solution-hardening in Fe-Cr-Ni austenitic stainless steels by various concentrations of carbon [11, 12, 51], nitrogen [11, 12, 51], and hydrogen [24, 33, 34, 38, 50] at ambient temperature.

The pronounced solid solution–hardening caused by H (hereinafter referred to as H–induced solid solution–hardening), and the associated increase in plastic deformation resistance, offer significant application potential. In components such as high–pressure gas pipelines—where the applied stress is maximized at the surface in contact with H_2 (the entry side of H)—this effect may serve not only to spontaneously strengthen the material and suppress fracture but also to enhance resistance against fatigue failure [26]. Nevertheless, despite similar phenomena having been reported in a wide range of FCC materials—including pure Ni [27–29], Ni–based alloys [21, 30, 31], austenitic steels [32–34], and more recently, high–entropy alloys [22, 35]—our understanding of the characteristics and underlying mechanisms of H–induced solid solution–hardening remains insufficient, even after more than half a century since research in this area began. In particular, considering the most fundamental principle that solid solution–hardening originates from the mechanical interactions between lattice strain fields around interstitials and dislocations [36, 37], the finding that H—despite having a much smaller atomic radius than C or N—can achieve comparable strengthening is seemingly anomalous. Elucidating such an anomaly is a critical issue for revisiting established theories of interstitial-induced solid solution–hardening in FCC alloys and for further approaching the essential nature of strengthening mechanisms. Since the aforementioned discovery, the present authors have continued research using both macroscopic mechanical testing and atomic–scale simulations. We aimed for comprehensively understanding the effects of H concentration, temperature, strain rate, and alloy composition on H–induced solid solution–hardening in Fe–Cr–Ni austenitic steels, and for constructing a unified model capable of explaining the dependencies on these parameters without contradiction [23, 24, 38–41]. The present paper provides, in relation to relevant literature, an overview of the latest insights we have accumulated and describes the concept of the H–induced solid solution–hardening model we have developed. Ultimately, the remaining research challenges are raised.

2. Phenomenological Characters of H–Induced Solid Solution–Hardening

2.1 Lattice strain and concentration–dependence

When segregation to lattice defects such as dislocations or grain boundaries is not taken into account, all three interstitial elements—carbon, nitrogen, and hydrogen—occupy octahedral interstitial sites (O–sites) in FCC lattice (Fig. 2). According to a simple rigid–sphere model, the radius of austenitic O–site in 300 series stainless steels is approximately 52–53 pm, whereas the covalent radii of carbon and nitrogen are relatively large, around 70 pm [42]. In practice, the bonding state and interactions between host metallic atoms and interstitial elements affect this approximation, leaving some doubt about its accuracy. However, X–ray diffraction has experimentally shown a lattice expansion of approximately $\Delta V = 8.6 \times 10^{-3}\,\mathrm{nm}^3$ per carbon or nitrogen atom in austenite [43]. Ohkubo *et al.* added various interstitial and substitutional elements to an austenitic steel primarily composed of Fe–17Cr–12Ni–0.8Mn (mass%). They reported a good correlation between the lattice constant change due to alloying elements and the amount of solid solution–hardening [13]. A similar trend is also clearly demonstrated in the book written by Marshall [44]. As will be discussed later, the influence of other factors, such as complexes formed between interstitial and substitutional atoms, has been pointed out [11, 12, 45, 46]. Nevertheless, it is an undeniable fact that lattice strain around carbon and nitrogen contributes to solid solution–hardening to a certain extent. According to the work by Slater, who estimated atomic radii based on experimentally determined interatomic distances in various crystal structures [42], the covalent radius of H is less than 30 pm (Fig. 2). The present authors performed neutron diffraction measurements on bulk specimens of Type310S (Fe–24Cr–19Ni) steel uniformly charged

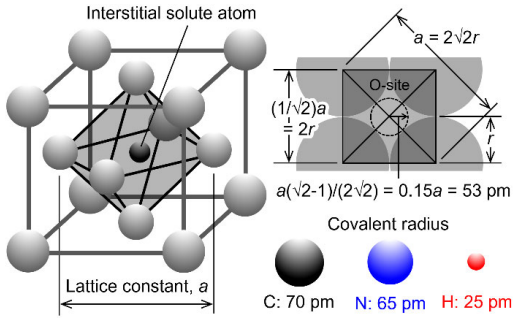

Fig. 2 Configuration of octahedral site (O-site) in FCC austenite lattice according to the simple rigid sphere model and covalent radius of interstitial solute atoms (C, N, H) [42]. (online color)

with 7600 at ppm H and revealed that the lattice expansion per H atom is $\Delta V = 2.27 \times 10^{-3}\,\mathrm{nm}^3$ [47]. This value is approximately one–quarter of the lattice expansion caused by carbon or nitrogen, almost consistent with both experimental [48] and atomistic simulation results [49] by other researchers.

Figure 1 summarizes the dependence of yield stress (0.2% proof stress) enhancement on solute H concentration, measured at room temperature in Fe–Cr–Ni austenitic steels over a wide range of compositions [24, 33, 34, 38, 50]. The experimental data for carbon and nitrogen [11, 12, 51] are included together. The amount of H–induced solid solution–hardening is linearly proportional to H concentration; although slightly lower than the strengthening by nitrogen, it is comparable to or even greater than that by carbon. This provides clear evidence that H–induced solid solution–hardening originates not only from lattice strain but also from other intrinsic factors. It should be noted that most of the data points in Fig. 1 were obtained from specimens uniformly charged with H *via* long–term exposure to high–temperature and high–pressure H_2 environments. The maximum H content that can be achieved by gaseous exposure is limited to below 10,000 at ppm (1 at%). In contrast, Abraham and Altstetter added up to 10 at% H to thin films of Type310S steel by cathodic charging and measured the yield stress [33]. In their data, the magnitude of strengthening tended to saturate when the H content exceeded 5 at%.

2.2 Effects of temperature and strain rate

The process in which a dislocation overcomes solute atoms as short–range (a few atomic spacings) obstacles—including their strain fields—is generally a thermally activated process aided by atomic vibration [52]. Accordingly, in addition to solute concentration, the parameters that have been investigated as factors influencing solid solution–hardening are the deformation temperature and strain rate (*i.e.*, allowable time to cause a certain amount of deformation).

Figure 3 shows the stress–strain curves and the temperature– and strain rate–dependences of the yield stress in Type310S steel (with the H concentration of 7300–7600 at ppm), obtained by the authors in the temperature range of 173–423 K [38]. As can be seen from Fig. 3(b), the yield stress increases monotonically with decreasing temperature, regardless of the presence or absence of H. This trend indicates that thermally activated processes contribute significantly to dislocation motion at the yield point in the Type310S steel. On the other hand, H–induced solid solution–hardening (*i.e.*, the gap of yield stress between H–charged and non–charged specimens) becomes significant at temperatures below 400 K (Fig. 3(c)). Although the amount of H–induced solid solution–hardening once tends to increase with decreasing temperature, it shows a peak around 300 K. A particularly notable feature is the influence of strain rate near 300 K; when the strain rate is decreased from 5×10^{-5}/s to 5×10^{-7}/s—equivalent to an increase in temperature in terms of thermal activation, the H–induced increase in yield stress is significantly reduced. However, when the strain rate is increased from 5×10^{-5}/s to 5×10^{-3}/s, the amount of solid solution–hardening again decreases, resulting in its peak around 5×10^{-5}/s. Such a phenomenon, in which solid solution–hardening is maximized near room temperature and at a specific strain rate, is a characteristic unique to H and not observable for C or N.

The non–monotonic dependence of solid solution–hardening on temperature and strain rate is often ascribed to solute diffusion [52–54]. Figure 4 presents the experimentally measured diffusion coefficients, D, of C [55–57], N [58–60], and H [8, 61, 62] in austenite, as well as their jump frequencies, v, calculated from the following equations.

$$D = D_0 \exp\left(-\frac{E_\mathrm{D}}{RT}\right) \tag{1}$$

$$v = \frac{24D}{a^2} \tag{2}$$

Here, D_0 is the pre–exponential factor, E_D is the diffusion activation energy, R is the gas constant, T is the absolute temperature, and a is the lattice constant. It should be noted that the reported diffusion coefficients for C and N are limited to temperatures above 700 K, and for H, to those above 400 K. Therefore, the data for temperatures below these ranges were extrapolated using D_0 and E_D measured at higher temperature domains. The diffusion of C and N in austenite is more than seven orders of magnitude slower than that of H, and their jump frequencies at 300 K are only about 10^{-4}/s or less. In contrast, the jump frequency of H at 300 K is as high as 10^5/s, indicating that H can diffuse through the material rapidly even at room temperature. The H diffusivity decreases

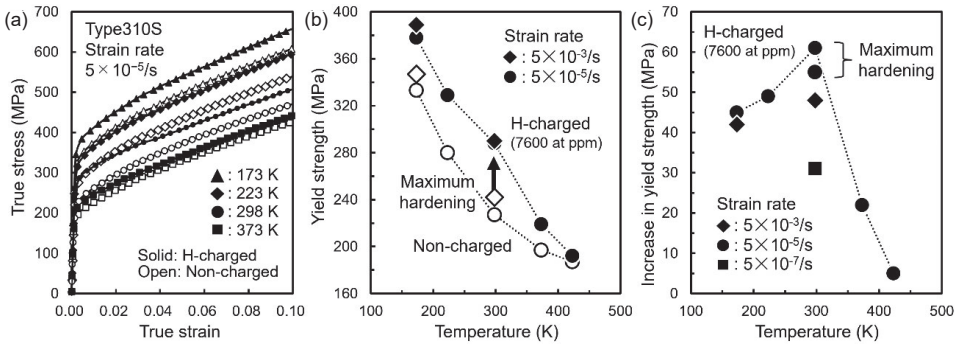

Fig. 3 Effects of temperature and strain rate on the characteristics of solid solution-hardening in Type310S (Fe-24Cr-19Ni) austenitic steel with (7300–7600 at ppm) and without hydrogen [38]. (a) true stress-strain curves; (b) yield strength as a function of temperature; and (c) hydrogen-induced increase in yield strength at different temperatures and strain rates.

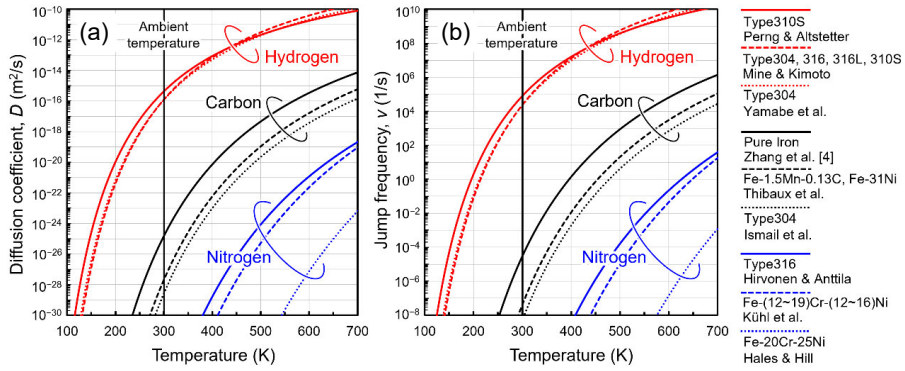

Fig. 4 (a) Diffusivity and (b) jump frequency of carbon [55–57], nitrogen [58–60], and hydrogen [8, 61, 62] in austenitic steels as a function of temperature, reproduced from the literature data. (online color)

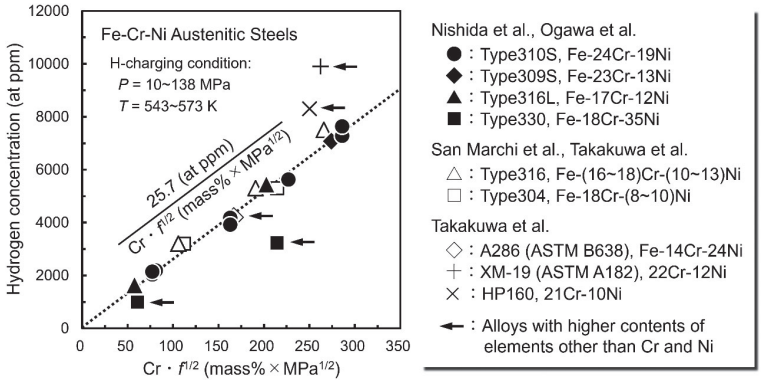

Fig. 5 Thermal equilibrium hydrogen concentration in Fe-Cr-Ni-based alloys as a function of the product between Cr content (mass%) and the fugacity of hydrogen gas [24, 34, 50, 64].

to the level of C and N at 300 K only when the temperature drops below 200 K. Notably, ≈200 K corresponds to the temperature range in Fig. 3(c) where the amount of H–induced solid solution–hardening begins to decrease from its maximum. This implies that dynamic H diffusion during deformation plays an important role in the H–induced solid solution–hardening at room temperature, although its detailed role will later be discussed. Owing to its practical significance, the following sections will primarily focus on the H–induced solid solution–hardening at room temperature.

2.3 Effects of alloy composition

The H–induced solid solution–hardening is linearly proportional to H concentration (Fig. 1). Thus, for effectively manifesting the solid solution–hardening by H supplied from the gaseous phase, the alloy must possess high H–solubility, capable of dissolving more H under a given temperature and gas pressure condition. In this regard, substitutional alloying elements in austenite are of key importance.

The thermal equilibrium H concentration, C_S, in metals under H_2 gas environment is determined by the basic Sieverts' law [63]:

$$C_S = Kf^{1/2} \tag{3}$$

where K is a material constant including the H_2 gas temperature and the H–absorption energy. f is the H_2 gas fugacity, which accounts for the deviation from ideal gas behavior due to pressurization [63]:

$$f = P\exp\left(\frac{Pb}{RT}\right) \tag{4}$$

In eq. (4), P is the H_2 pressure, and b is a constant ($15.84\,cm^3/mol$ [63]). In general, the temperature–dependence of K is weak. Therefore, the equilibrium H concentration, C_S, in H_2 at a given temperature and pressure can be approximated as being proportional to $f^{1/2}$.

The present authors investigated the H–solubility in austenitic steels with various Cr and Ni percentages under controlled H_2 environment, identifying a strong interrelation between the equilibrium H concentration and Cr content [24]. Figure 5 presents a compilation of H–solubility data obtained from the authors' own studies [24, 64] and from the literature [34, 50, 64], in which the product of Cr content (mass%) and $f^{1/2}$ is used as a parameter predominating H–solubility. The H–solubility exhibits a nearly proportional relationship with $Cr \cdot f^{1/2}$, and the data from various alloys notably converge into a unified straight line. Although several materials, *e.g.*, Type330 and XM19, deviate from the linearity, these alloys contain relatively large amounts of extra elements such as Si, Mn, and Mo in addition to Fe–Cr–Ni. It is thus presumed that the H–solubility in these specific alloys might involve some non–negligible influences of extra elements other than Cr.

In order to rationalize the correlation between Cr content and H–solubility, Moriyama *et al.* employed first–principles calculations [41, 65]. They substituted some of the six Fe atoms surrounding an O–site in FCC iron with Cr/Ni,

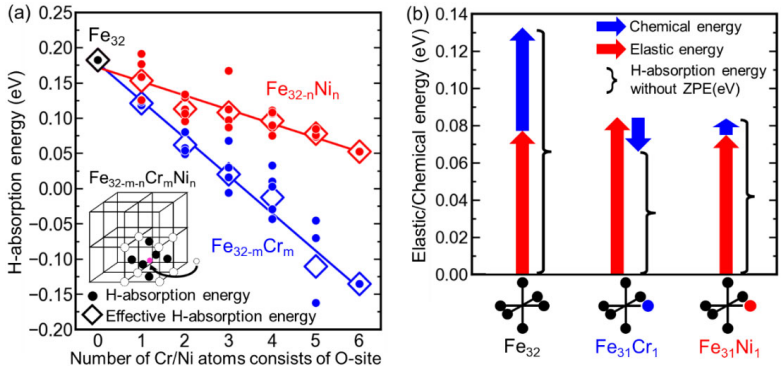

Fig. 6 Change in (a) H-absorption energy, effective average of H-absorption energy (effective H-absorption energy), (b) elastic energy, and chemical energy when Fe atoms surrounding an O-site are replaced by Cr and Ni. The round and diamond in (a) represent the H-absorption energy and the effective H-absorption energy, respectively. Red and blue arrows in (b) show elastic and chemical energy, respectively [41, 65]. (online color)

investigating the corresponding changes in H–absorption energy, E_{ab}, (the energy required to dissolve one H atom in O–site). Figure 6 depicts the variations in E_{ab} due to Cr/Ni substitutions, as well as the respective changes in the elastic energy (mechanical strain energy associated with the insertion of H) and chemical energy (energy arising from changes in electron density) that constitute E_{ab}. As seen in Fig. 6(a), E_{ab} tends to decrease with either Ni or Cr substitution, wherein Cr exhibits a markedly greater impact. Furthermore, in Fig. 6(b), chemical energy is significantly reduced, particularly by Cr, while its effect on mechanical energy is marginal. These results clearly indicate a strong electrochemical affinity between H and Cr. That is, increasing Cr content should enhance H–solubility, rationalizing the experimental trend in Fig. 5. Similar tendencies—albeit to varying degrees—have also been observed for other substitutional elements such as Mn and Al [66, 67]. In the context of alloy design aimed at effective utilization of H–induced solid solution–hardening, these computational information on the interactions between H and substitutional elements is expected to become increasingly important. From an experimental standpoint, measurements of internal friction are also of interest. Asano *et al.* [68, 69] and Gavriljuk *et al.* [70] discovered the Snoek–type relaxation peaks in H–charged Fe–Ni, Fe–Cr–Ni, and Fe–Cr–Ni–Mn alloys. The latter authors attributed these peaks to tetragonal distortion due to interactions between H and substitutional elements [70].

In accordance with the trend in Fig. 1, alloys with higher Cr content inevitably exhibit larger solid solution–hardening when H is introduced under specific gas pressure and temperature conditions. It remains unclear whether such strengthening is solely a consequence of increased H concentration itself or involves some influences of H–Cr interactions. Aiming at the practical utilization and comprehensive understanding of H–induced solid solution–hardening, this point awaits further elucidation in future studies.

3. H–Dislocation Interactions Controlling the Solid Solution–Hardening

Section 2 overviewed the previous experimental and analytical findings and characteristic features concerning the dependencies of H–induced solid solution–hardening on H concentration, temperature, strain rate, and alloy composition. In Section 3, the discussion will shift toward the mechanisms underlying such H–induced solid solution–hardening. The mechanistic model to be ultimately established must be capable of explaining, without contradiction, all the aspects of H–induced solid solution–hardening enumerated in Section 2. In particular, the peak of solid solution–hardening at room temperature and at a specific strain rate (Fig. 3) infers the importance of dynamic H–diffusion during deformation.

Just as carbon forms Cottrell atmosphere [71] within its diffusible temperature range, an extreme diffusivity of H (Fig. 4) allows their short time segregation to dislocation cores or stress fields even around room temperature [2, 72]. When strain rate (*i.e.*, dislocation velocity) is sufficiently low, those segregated H can migrate through the material with the moving dislocations. Although such coordinative motion has not directly been visualized, it has been substantiated through various indirect experiments (such as *in–situ* H–permeation tests during deformation [73]) and atomistic simulations [74].

3.1 *Solute drag* of H–atmosphere

3.1.1 Theoretical prediction

Cottrell and Jaswon were the first to point out, based on theoretical calculations, that a solute atmosphere dragged by a moving dislocation can act as a resistance to dislocation glide—*solute drag* [75]. Their theory was subsequently advanced by Hirth *et al.* [37, 76] and Yoshinaga *et al.* [77, 78], leading to specific formulae that relate the solute distribution within the atmosphere to the dislocation velocity, v_d, solute concentration, and the magnitude of drag resistance. More recently, the applicability of these classical theories to H in austenite has been explored by Sills *et al.* [79, 80]. In Section 3.1, we discuss this *solute drag* phenomenon by solely placing our focus on the elastic stress–strain fields outside the dislocation core, where continuum mechanics approximation holds. The issue of more localized interactions between dislocation core and H will be addressed in the following Section 3.2.

Sills *et al.* assumed a steady–state dislocation motion and introduced the following parameter Q as a dimensionless dislocation velocity that governs the contribution of the atmosphere to *solute drag* [80]:

$$Q = \frac{v_d \beta}{4DkT} \tag{5}$$

where k is the Boltzmann constant, and β is solute–dislocation interaction parameter, which includes the volume expansion ΔV caused by a solute atom. The presence and magnitude of the drag force for a given solute species and temperature are determined by the parameter Q. According to their analysis, the drag force emerges within the range of approximately $0.01 < Q < 100$. It reaches its maximum near $Q = 1$, decreasing as Q increases or decreases beyond this criterion [80]. Meanwhile, when $Q > 100$ or $Q < 0.01$, the dislocation leaves the atmosphere behind (breakaway limit) or the atmosphere follows the dislocation while maintaining its equilibrium distribution (equilibrium limit), providing no drag force in either case. By substituting eq. (5) into Orowan equation, which relates mobile dislocation density ρ_m and strain rate $\dot{\varepsilon}$ as $\dot{\varepsilon} = \rho_m b v_d / M_T$ (b is the Burgers vector and M_T is the Taylor factor), the following eq. (6) is obtained:

$$\dot{\varepsilon} = \frac{4QDkT}{M_T \beta} \rho_m b \tag{6}$$

Figure 7 depicts the transitions of $Q = 0.01$, 1, and 100 criteria for three different mobile dislocation densities ($\rho_m = 10^{11}$, 10^{12}, $10^{13}/m^2$) on the temperature–strain rate space. These curves were calculated based on eqs. (5) and (6) by using the H diffusion coefficient in austenitic steels (Fig. 4) and the volume expansion per H atom, ΔV (see Ref. [38] for details). One drawback when comparing Fig. 4 with practical experimental data is the difficulty in measuring actual ρ_m. Nevertheless, in FCC materials (*e.g.*, Cu [81] and Type304 steel [82]), it has been shown—based on Orowan equation and Bailey–Hirsch relationship ($\sigma = \alpha G b \rho$: σ is the flow stress, α is a constant dependent on dislocation character and material, G is shear modulus, and ρ is total dislocation density)—that ρ_m increases sharply from the order of $10^{11}/m^2$ to $10^{13}/m^2$ or more around the yield point. Therefore, Fig. 7(a)–(c) likely represents the successive behavior before and after the onset of yielding. In Fig. 7, the strain rate of 5×10^{-5}/s, at which H–induced solid solution–hardening reaches its maximum, is located close to $Q = 1$ line around 300 K. As ρ_m exceeds $10^{13}/m^2$ after yielding, the situation shifts toward $Q = 0.01$ side. This result indicates that the atmosphere drag force reaches its maximum at yielding and then diminishes as deformation progresses. Although these calculations are quite simplified, *solute drag* of H atmosphere seems to contribute significantly to the appearance of the yield stress peak in Fig. 3(c). Furthermore, in conventional theoretical formulations, there exists a proportionality between the atmosphere drag force and the average solute concentration [37]. Such a proportionality may be one of the reasons why solid solution–hardening at room temperature linearly augments with H concentration (Fig. 1).

3.1.2 Experimental evidence for the contribution of *solute drag*

(1) Fluctuation of the strengthening around yield stress

In this subsection, we introduce several experimental facts substantiating the *solute drag* of H atmosphere that was suggested by the theoretical predictions. Figure 8 shows the flow stress gap between H–charged and non–charged specimens (*i.e.*, the amount of solid solution–hardening), plotted against true strain, for the same Type310S steel presented in Fig. 3 [38]. Above 373 K, H–induced solid solution–hardening continues to act even after yielding. However, an eye–catching behavior is observed at 298 K under a strain rate of 5×10^{-5}/s: from the yielding up to a true strain of approximately 0.05, the amount of solid solution–hardening gradually decreases from ≈60 MPa to ≈30 MPa. This is reasonably understood in light of the discussion above (Fig. 7)—under these deformation conditions, the Q value transitions from 1 to 0.01 after yielding, gradually diminishing the drag force. In other words, the decrease in solid solution–hardening with the magnitude of ≈30 MPa possibly corresponds to the contribution of the drag force from the H atmosphere. Supporting this interpretation,

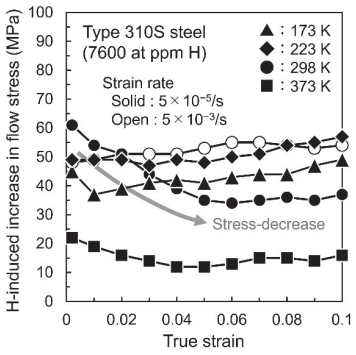

Fig. 8 Magnitude of solid solution-hardening in Type310S (Fe-24Cr-19Ni) steel containing 7600 at ppm H at various temperatures and strain rate [38].

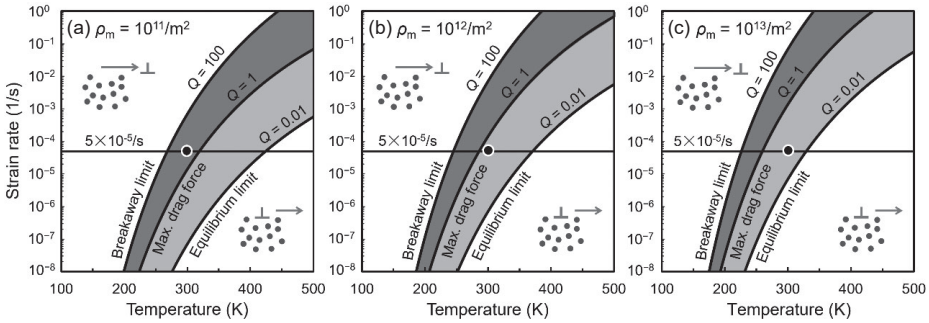

Fig. 7 Strain rate characterizing dynamic hydrogen-dislocation interactions, which are defined by $Q = 100$, 1, and 0.01 in eq. (5) and (6), as a function of temperature [38]. Mobile dislocation density, ρ_m, is parametrically set as (a) 10^{11}, (b) 10^{12}, and (c) $10^{13}/m^2$. The hatched areas denote the temperature and strain rate ranges where drag force by solute atmosphere is feasible to emerge.

no continuous and distinct decrease in the solid solution–hardening after yielding is observed when the pre–yield state lies outside or close to the outer boundaries of the hatched region in Fig. 7 (Fig. 8).

The reduced magnitude of solid solution–hardening after yielding could be recognized in Fig. 8, where the flow stress was plotted in a differential form. However, on the actual stress–strain curves, the influence of work–hardening overwhelms, making the total flow stress increase monotonically with strain. Nevertheless, although it is not visible on the stress–strain curves, the effect of reduced solid solution–hardening due to the loss of drag force can be observed as a temporary reduction in the post–yield work–hardening rate [38]. Nishida *et al.* confirmed such characteristic work–hardening behavior not only in Type310S steel but also in several other steel grades, including Type309S and Type316L [24]. Based on these facts, *solute drag* of H atmosphere is likely a universal phenomenon manifesting in Fe–Cr–Ni–based austenitic steels. Recently, McDowell *et al.* performed crystal plasticity finite element simulations incorporating the effects of solute H on Type316L steel. They accurately reproduced experimental stress–strain curves by taking the variation in drag force around the yield point into account [83].

The stress drop caused by a rapid increase in mobile dislocation density and a concomitant decrease in dislocation velocity—observable also in BCC metals and covalent crystals such as LiF—can be ascribed to the yield point theory developed by Johnston and Gilman (J–G) [84]. The stress dependence of dislocation velocity generally follows a power law relationship, $v_d = A\tau^m$ (where τ is the shear stress and A and m are material constants). When A is large and dislocation mobility is high as for FCC metals, the microscopic plastic strain rate promptly exceeds the externally imposed macroscopic strain rate once the stress exceeds a critical level so that dislocation motion and multiplication commence. As a result, a stress drop in J–G mechanism does not occur, rendering the yielding behavior predominated by the dislocation multiplication process [85]. Nevertheless, Horiuchi and Yoshinaga found a distinct yield point in Al–Mg alloys due to a reduction in dislocation mobility at high temperatures where *solute drag* is operative and work–hardening is minimal. In particular, they termed this unusual phenomenon as "high temperature yield point" [86, 87]. Possibly, Fig. 8 suggests that the phenomenon identified by Yoshinaga *et al.* manifested at room temperature owing to the diffusion of H—the reduction in dislocation mobility (*i.e.*, a decrease in the coefficient A) caused by the H atmosphere drag might transform the multiplication–controlled yielding to mobility–controlled. Indeed, in the experiment by Abraham and Altstetter [33], where more than 1 at% H was introduced into Type310S steel *via* cathodic charging, a clear yield drop appeared at room temperature and a strain rate of 5.5×10^{-5}/s. In their case, the stress drop seen in Fig. 8 might become more pronounced thanks to the higher H concentration. It should be noted that, as for the yield point in carbon steels, a yield drop can also appear by the sudden breakaway of dislocations from the pinning by solute atmospheres. However, in such a circumstance, the stress drop should occur regardless of strain rate. At room temperature in Fig. 8, the stress drop rather disappears at a high strain rate of 5×10^{-3}/s. This indicates that the dislocation pinning by the H atmosphere is not significant at room temperature.

Another noteworthy point when discussing the post–yielding deformation is the possible effect of H on dislocation accumulation and associated work–hardening. In some FCC materials, such as pure Ni and Ni–based alloys, H–induced changes in dislocation structures and dislocation cell size have been observed [21, 88–90], making their influence on the flow stress after yielding not negligible. However, in the authors' own investigations of austenitic steels—including transmission electron microscopy (TEM) [39], dislocation density measurements by neutron diffraction [47], and hardness measurements after H–desorption from the deformed samples [91]—no significant H–effect on dislocation accumulation or structural evolution has been identified in the low to medium (at least ~20%) strain. Therefore, in Fe–Cr–Ni alloys targeted in this paper, the change in flow behavior after yielding can reasonably be approximated as being solely governed by the H–effect on the mobility of individual dislocations.

(2) Variation in strain rate sensitivity

An additional experiment that provided the evidence for *solute drag* is the measurement of the strain rate sensitivity, S. The authors conducted strain rate jump tests at room temperature on Type310S steel charged with 7600 at ppm H [40]. Figure 9(a) shows representative stress–strain curves measured at a base strain rate (*i.e.*, the strain rate before it was increased tenfold) of 10^{-4}/s. On these stress–strain curves, sharp stress–rises correspond to the moments when the strain rate was suddenly increased tenfold from the base, while sudden stress–drops reflect the return from the elevated rate to the base. These stress changes were measured under multiple base strain rates, and the increase in flow stress $\partial\tau$ upon strain rate jump (converted from normal stress to shear stress using the Taylor factor of FCC polycrystals, $M_T = 3.06$) was plotted against true strain in the form of $S = \partial\tau/\partial \ln \dot{\varepsilon}$. The results are shown in Fig. 9(b). The H–charged specimens generally exhibit larger S compared to non–charged specimens, the reason for which will be discussed later.

In H–charged specimens, one may notice in Fig. 9(b) that the strain rate sensitivity, S, strongly depends on both the base strain rate and true strain. Particularly, under the base strain rates of 10^{-3}/s and 10^{-4}/s, S evolves sharply from ≈1 MPa to ≈4 MPa over the strain range from just after yielding up to ≈0.1. To correlate this behavior to *solute drag*, Fig. 10(a) reorganizes Fig. 7 by focusing on room temperature and converting the horizontal axis to mobile dislocation density. If the mobile dislocation density at the post–yield small strain is $\rho_m \sim 10^{12}/m^2$, and in the later deformation stage is $10^{13}/m^2$ order, rapid increases in strain rate by a factor of 10 from the bases of 10^{-3}, 10^{-4}, and 10^{-5}/s correspond to the upward arrows indicated in Fig. 10(a). When these arrows are transferred to the drag force versus strain rate curve, one yields schematic diagrams like Figs. 10(b) and (c). As of particular interest here, in low strain domain with the base strain rates of 10^{-3}/s and 10^{-4}/s, the drag force drops sharply in response to the strain rate jump (Fig. 10(b)). Given that the

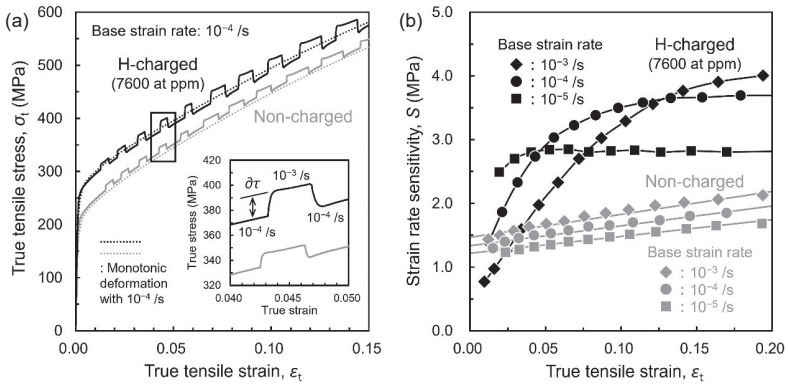

Fig. 9 (a) Examples of true stress-strain curves during strain rate jump test of Type310S steel at room temperature and (b) the measured strain rate sensitivity as a function of strain [40].

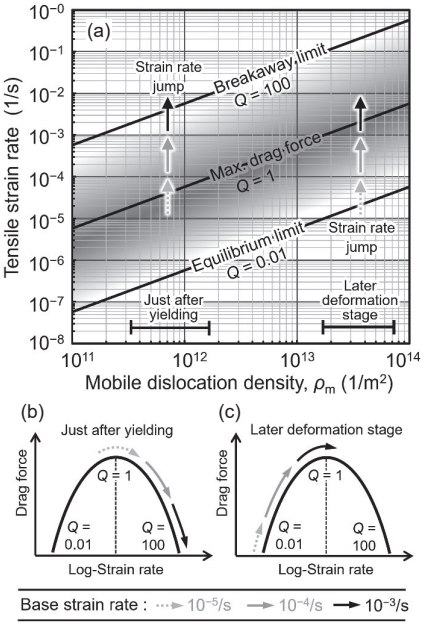

Fig. 10 (a) Strain rate range, where H atmosphere exerts drag force against dislocation motion, as a function of mobile dislocation density. (b) and (c) schematically correlate the situations in strain rate jump tests under different base strain rate with the magnitude of drag force [40].

intrinsic S in the H–charged specimen without *solute drag* effect is 3 to 4 MPa (the origin of this large S will be discussed later) measured at the later deformation stage, the low S of approximately 1 MPa in the early deformation stage in Fig. 9(b) should reflect the value in which loss of drag force due to the strain rate jump is subtracted. Indeed, under the base strain rate of 10^{-5}/s, where little change in drag force is anticipated even after a strain rate jump, the S in the early deformation stage is quite stable (Fig. 9(b)). In contrast, at the later deformation stage depicted in Fig. 10(c), the tenfold increase in strain rate from 10^{-3}/s or 10^{-4}/s oppositely results in an increase in drag force. This implies that the contribution of drag force to S gradually transitions from negative to positive as deformation proceeds, providing a consistent explanation for the evolution of S in Fig. 9(b). At the base strain rate of 10^{-3}/s, the initial deformation stage is closer to the boundary of $Q = 100$ (Fig. 10(a)). Thus, compared to the 10^{-4}/s case, a larger strain is required to render such S–contribution from negative to positive. For this reason, the curve of the H–charged specimen at 10^{-3}/s exhibits a rightward–shift from the one at 10^{-4}/s (Fig. 9(b)), with a rapid increase in S at a higher strain level.

3.2 Thermal activation process of dislocation motion

The foregoing discussion substantiated the significance of H atmosphere *solute drag* in the yield stress peak observed near room temperature and a strain rate of $\approx 5 \times 10^{-5}$/s. On the other hand, even in the later deformation stages where drag force diminishes, or at a strain rate of 5×10^{-7}/s where drag force is already zero at the yielding (Fig. 10(a)), the H–induced solid solution–hardening still remains substantial (Fig. 3(c)). Furthermore, as noted in Fig. 9(b), the S value—the stress increment *via* strain rate jump—is greater in H–charged specimens than in non–charged ones. This indicates that, in addition to the interaction between H atmosphere and dislocations, individual H atoms contribute to solid solution–hardening by playing the role of short–range (thermal) obstacles.

3.2.1 Dislocation motion *via* overcoming short–range (thermal) obstacles

As illustrated schematically in Fig. 11, when a dislocation moves across a slip plane dispersed with short–range obstacles, it generally overcomes the obstacles with the aid of both externally applied stress and atomic thermal vibration [52]. The energy that must be supplied by thermal vibration during this process, ΔG, is expressed as a function of shear stress, τ^*, acting on the dislocation line, as is also evident from Fig. 11(c):

$$\Delta G = \Delta G_0 - \tau^* V \tag{7}$$

where ΔG_0 is the intrinsic activation energy of the obstacle at $\tau^* = 0$, and V is the activation volume. The activation volume—$V = bdL$—is defined as the product of Burgers vector, b, and the area swept by dislocation during thermal activation process (activation area, A: the width of an individual obstacle, d, multiplied by the average obstacle interspacing, L) (Fig. 11) [92]. The shear stress τ^* (also referred to as the effective stress) is given by subtracting the internal stress, τ_μ—stress component independent of temperature and strain rate—from the total flow stress applied to the material, τ—$\tau = \tau^* + \tau_\mu$. From eq. (7), the following relationship is self–evident:

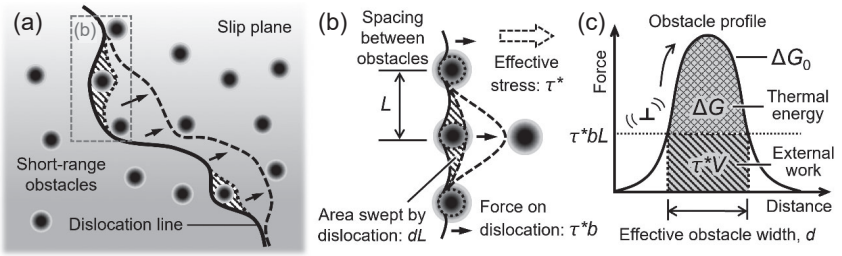

Fig. 11 (a) Schematic drawing of the movement of a dislocation line through the field of short-range obstacles on its slip plane. (b) magnifies the process overcoming single obstacle *via* thermal activation, while (c) denotes the side view of (b) and the physical sense of activation parameters.

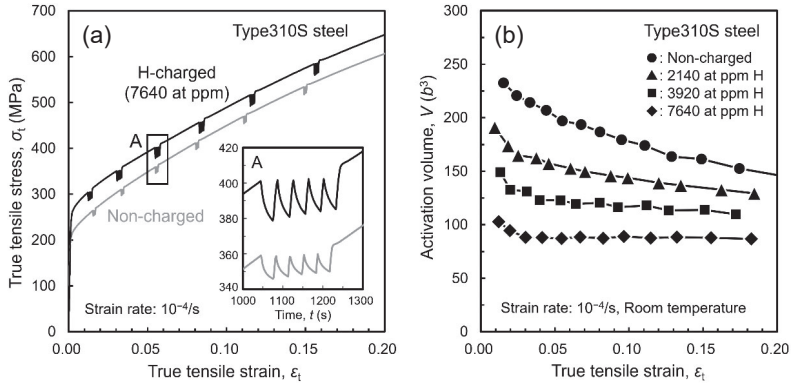

Fig. 12 (a) True stress-strain curves during the stress-relaxation tests of Type310S steel at room temperature and (b) the measured activation volume under various hydrogen concentrations [39].

$$V = -\left.\frac{\partial \Delta G}{\partial \tau^*}\right|_T \tag{8}$$

On the other hand, the shear strain rate $\dot{\gamma}$ of the crystal under effective stress, τ^*, and thermal energy, ΔG, follows the Arrhenius–type rate equation [36, 52], where $\dot{\gamma}_0$ is a constant including the vibrational frequency of the dislocation segment, the obstacle interspacing, L, and the mobile dislocation density, ρ_m:

$$\dot{\gamma} = \dot{\gamma}_0 \exp\left(-\frac{\Delta G}{kT}\right) \tag{9}$$

Taking the logarithm of both sides of eq. (9) and rearranging with respect to ΔG, then differentiating by τ^* according to eq. (8), one yields:

$$\frac{kT}{V} = \frac{\partial \tau^*}{\partial \ln \dot{\gamma}} = \frac{\partial \tau}{\partial \ln \dot{\gamma}} \tag{10}$$

Here, the right–hand side of eq. (10) is equivalent to the strain rate sensitivity, $S = \partial\tau/\partial \ln \dot{\varepsilon}$, defined in Section 3.1.2 (2). An essential theoretical relationship is now reached: V is inversely proportional to S. Note that in eq. (10), τ^* is replaced by τ since the strain rate–derivative of τ_μ should be zero.

3.2.2 Reduction in activation volume due to H

To understand the nature of short–range obstacles, measurement of activation volume, V—information on the size and distribution of obstacles—is useful. For this purpose, thermal activation analyses utilizing the transient of plastic deformation (*e.g.*, stress relaxation and creep tests) have been employed [52, 93]. Figure 12 shows an example of a stress–strain curve obtained from a stress relaxation test conducted by the authors on Type310S steel containing approximately 7600 at ppm H, together with the activation volume, V, determined by fitting the relaxation curve to a theoretical equation [39] (for the details for calculating V, refer to [94, 95]). A characteristic feature in the H–charged specimen is that the amount of stress relaxation within a given period (here, 30 seconds) is obviously larger than that in the non–charged specimen. Moreover, as a general behavior of FCC materials, V tends to decrease with increasing strain. However, in the H–charged specimen, the strain–dependence of V becomes weaker with increasing H concentration, besides the overall decrease in V throughout the deformation process. According to eq. (10), the trend in Fig. 12(b) indicates the increase in strain rate sensitivity, S, caused by H. This tendency is a direct reproduction of the overall increase in S due to H shown in Fig. 9(b).

As for the specific values of V, when the obstacles are lattice friction such as Peierls potential, V is usually less than $100b^3$; for solute atoms, it ranges from several tens to hundreds of b^3; and for dislocation–dislocation intersections, it ranges from several hundreds to thousands of b^3 [85, 96]. Considering that the Peierls potential in FCC crystal is negligibly small, the measured values of 100–200b^3 in Fig. 12(b) indicate that solute atoms—including H and other alloying elements—as well as forest dislocations, act as the rate–controlling obstacles.

3.2.3 Extracting H–effects as short–range obstacles

In Section 3.2.1, thermally activated dislocation motion was discussed for the case where the obstacle species is single. However, in practice, multiple obstacle types are often

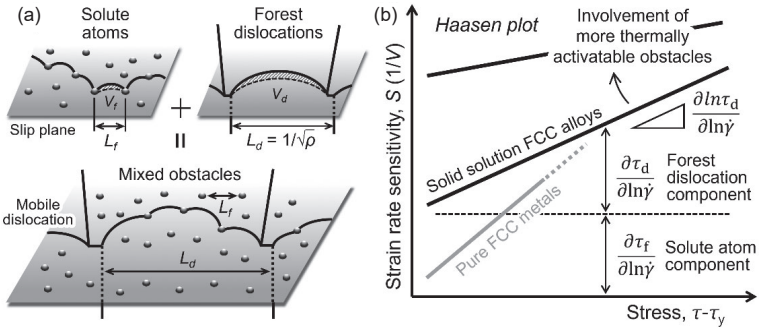

Fig. 13 Schematic drawings of (a) the movement of dislocations through the field of two different types of obstacles (*e.g.*, solute atoms and forest dislocations) and (b) corresponding *Haasen plot*, where strain rate sensitivity (or inverse activation volume) is plotted against stress.

present, besides additional obstacles, *e.g.*, forest dislocations, are newly introduced during deformation (Fig. 13(a)). To clarify the role of H within such a complex situation, it is necessary to extract the pure effect of H on deformation behavior by screening other factors that influence the activation volume.

Kocks [97] and Mulford [98], focusing on the decomposing method of effective stress in the work of Haasen [99], proposed a way to separate the contributions from individual obstacles in a system containing multiple obstacle types. In the case where there are two types of short–range obstacles, they first assumed that the flow stresses arising from each obstacle type, τ_1 and τ_2, follow a linear additivity.

$$\tau = \tau_1 + \tau_2 \tag{11}$$

The additivity holds only in a specific situation. Nevertheless, the combination of forest dislocations with high concentrations of solutes (Fig. 13(a)) represents a typical example of such a case [92, 97, 100]. In what follows, the contribution from solutes is denoted as τ_f, and that from forest dislocations as τ_d. When total flow stress τ is a sum of τ_f and τ_d, the additivity also holds for strain rate sensitivity, S—a derivative of τ.

$$S = \frac{\partial \tau}{\partial \ln \dot{\gamma}} = \frac{\partial \tau_f}{\partial \ln \dot{\gamma}} + \frac{\partial \tau_d}{\partial \ln \dot{\gamma}} = \frac{\partial \tau_f}{\partial \ln \dot{\gamma}} + \frac{\partial \ln \tau_d}{\partial \ln \dot{\gamma}} \tau_d \tag{12}$$

Note that in the transformation of the second term of eq. (12), $\partial \ln \tau_d / \partial \ln \dot{\gamma} = (\partial \ln \tau_d / \partial \tau_d)(\partial \tau_d / \partial \ln \dot{\gamma}) = (1/\tau_d)(\partial \tau_d / \partial \ln \dot{\gamma})$. Since τ_d corresponds to the increase in flow stress due to work–hardening, the total strain rate sensitivity S can be expressed as follows by taking the yield stress as τ_y:

$$S = \frac{\partial \tau_f}{\partial \ln \dot{\gamma}} + \frac{\partial \ln \tau_d}{\partial \ln \dot{\gamma}} (\tau - \tau_y) \tag{13}$$

Furthermore, considering eq. (10) that $S \propto 1/V$, eq. (13) can be transformed as follows by denoting the solutes and forest dislocation components of activation volume as V_f and V_d, respectively:

$$\frac{1}{V} = \frac{1}{V_f} + \frac{1}{\tau_d V_d} (\tau - \tau_y) \tag{14}$$

Therefore, if the reciprocal of V measured during a tensile deformation—or S, which is proportional to $1/V$—is plotted against $\tau - \tau_y$, the intercept on the vertical axis reflects the influence of solutes on V, while the slope represents the contribution of forest dislocations. This method is known as the *Haasen plot* (Fig. 13(b)). It has been widely applied to the decomposition of strengthening mechanisms in various materials, including solid solution–strengthened and precipitation–hardened alloys [98, 101–105].

In FCC pure metals such as Ni and Ag, where yield stress is low and no short–range obstacles other than forest dislocations are present—that is, where the first term of eqs. (13) and (14) ≈ 0—the *Haasen plot* becomes a straight line passing through the origin [98, 106]. This linearity is referred to as the Cottrell–Stokes law [106, 107]. The linearity of the *Haasen plot* implies that the product $\tau_d V_d$ in eq. (14) is constant. It is because the increment of flow stress by work–hardening, τ_d, is proportional to $\rho^{1/2}$ according to the Bailey–Hirsch equation, while the forest dislocation component of the activation volume, V_d, is proportional to the average dislocation interspacing, $\rho^{-1/2}$ (see Fig. 13(a)).

Figure 14 shows an example of *Haasen plot* for Type310S steel [39], obtained by converting the V measured in the stress relaxation test (Fig. 12) into S using eq. (10). In the non–charged case, the *Haasen plot* becomes a straight line with a positive intercept on the vertical axis, satisfying the Cottrell–Stokes law. This positive intercept—that is, the first term of eqs. (13) and (14)—can be attributed to the combined contributions of alloying elements originally contained in the alloy, *i.e.*, Cr, Ni, Si, and C. In contrast, for the H–charged specimens, although the linearity of *Haasen plot* holds, two distinctions appear with increasing H concentration: (i) an increase in intercept, and (ii) a decrease in slope. Among these, (i) the increased intercept reflects the overlapping effect of H that acts as additional short–range obstacles, superimposed on the material's intrinsic positive intercept. By taking this intercept change from the non–charged condition and its dependence on H concentration as indicators, the intrinsic H–effect can be discussed while screening the influences of other alloying elements and forest dislocations.

The increase in *Haasen plot* intercept corresponds to a decrease in V_f, associated with thermally activated movement of individual dislocations (eq. (14)). Physically, it implies that either or both of the obstacle size, d, and their interspacing, L, (Fig. 11) have decreased. In other words, thermal activation process that controls plastic deformation has become a more localized event after the introduction of H. Although (ii) the decrease in slope is not yet fully understood, it might result from a reduced contribution of forest dislocations to thermally activated deformation. That is, the rate–controlling

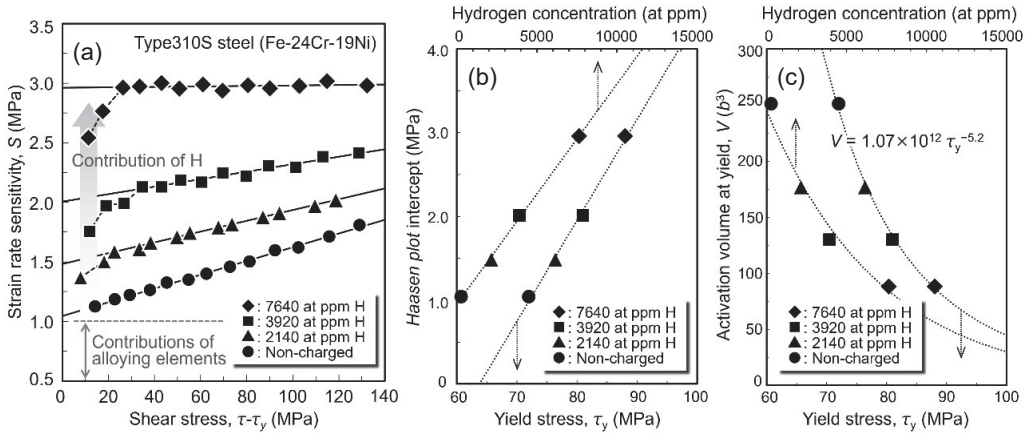

Fig. 14 *Haasen plot* of non-charged and hydrogen-charged Type310S steel at room temperature. The plotted strain rate sensitivity, *S*, were obtained by converting the activation volume in Fig. 12(b) *via* eq. (10) [39]. (b) indicates the ordinate intercept of *Haasen plot* in (a). The plot points in (b) were converted into activation volume *via* eq. (10) and reproduced in (c).

mechanism has shifted to the process in which dislocations overcome a newly introduced obstacle: H.

3.2.4 *Stress equivalence* of H–induced solid solution–hardening and activation volume

As shown in Fig. 14(b), the *Haasen plot* intercept increases linearly with both yield stress and H concentration. In addition, an interesting phenomenon here is the correlation between yield stress and activation volume V_f calculated from these S values at the intercepts [39]. Figure 14(c) shows a graph in which the intercepts in Fig. 14(a) are converted into activation volumes using eq. (10) and plotted as functions of H concentration and yield stress. The V_f at yielding follows a power–law relationship with yield stress, converging all data points for both H–charged and non–charged specimens onto a unified curve.

Basinski *et al.* investigated the relationship between yield stress and activation volume in Cu alloys containing various species and concentrations of substitutional elements. They reported that even when solute species and concentrations differ, materials possessing an equivalent activation volume also exhibit mutually identical yield stresses [108]. They termed this phenomenon "stress equivalence" and further demonstrated that, at a constant deformation temperature, the yield stress and activation volume of all alloys follow a power–law relationship like Fig. 14(c). Figure 14(c) can thus be interpreted as a manifestation of such "stress equivalence" in the yield stress variation induced by H in austenitic steel. The dependence of activation volume solely on the yield stress and its independence on solute concentration necessitates a correction of the conventional thermal activation model, in which a dislocation surmounts individual obstacles one by one (Fig. 11). In this regard, Basinski *et al.* emphasized that the experimentally measured activation volumes are always larger than the values estimated from the average interspacing of solutes—that is, multiple solute atoms may simultaneously be involved in each thermal activation event [108]. Indeed, in austenitic steels examined in our own study, the V values—on the order of $100b^3$—are much larger than expected from the mean interspacing of H ($\approx 10b$ [39]) for the present concentration range (~7600 at ppm). The potential thermally activated mechanisms responsible for these macroscopic trends, discussed in Sections 3.2.1–3.2.4 will be addressed in the following Sections 3.2.5–3.2.6.

It should be noted that the yield stress on the horizontal axes in Fig. 14(b) and (c) includes the influence of *solute drag*. However, as described in Section 3.1.1, the magnitude of such a drag force is also proportional to the average H concentration. Therefore, even if the contribution of *solute drag* were subtracted from the yield stress, the experimental tendencies in Fig. 14(b) and (c) would remain unchanged.

3.2.5 Thermal activation model for H–induced solid solution–hardening: Application of *trough model*

Theories of solid solution–hardening originated with the lattice friction model proposed by Mott and Nabarro [109], subsequently developed through the point–like obstacle model by Friedel–Fleischer [110, 111] and Labusch's model considering simultaneous interactions with plural obstacles [112]. Although these theories can adequately describe solid solution–hardening in certain alloys, depending on the solute concentration and solute–dislocation interaction force, they unfortunately cannot provide a rational explanation for "stress equivalence". Later, Kocks applied Fisher's theory [113], which modeled the breakaway of a dislocation line from a row of segregated solutes. He attempted a physical interpretation of "stress equivalence" by considering a specific process, in which a dislocation line bonded with dispersed solute atoms bows–out a short segment *via* thermal activation (Fig. 15(a)) [54]. In his model, the bonded stable position of the dislocation line is approximated by a triangular potential, regarding the pre–bowing dislocation as lying at the bottom of the potential trough (Fig. 15(b)); thus, he referred to his model as the *trough model*. In this framework, the dominant factors determining the trough depth are the solute–dislocation interaction energy per unit length and the corresponding reduction in dislocation's self–energy and line tension. These quantities are governed by the bonding strength between the individual solute and dislocation (*i.e.*, solute species) and by the solute density along the dislocation line (*i.e.*, solute concentration). Conversely, even for different solute species and concentrations, the bow–out process under a given applied stress becomes equivalent if the total reduction in self–energy is fixed. This inherently results in the same activation volume.

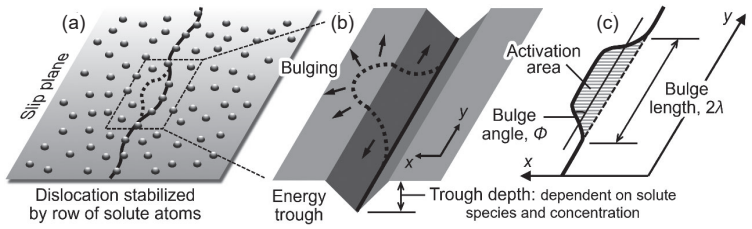

Fig. 15 Schematic drawings of the *trough model* for solid solution-hardening proposed by Kocks [54]. (a) Dislocation line, stabilized by row of solute atoms on the slip plane, tries to move *via* (b) bulging a small segment. The initial stabilized state is assumed as (b) the bottom of energy trough. The parameters characterizing the bulge are shown in (c).

For the application of *trough model*, the moving dislocation line must interact frequently with solute atoms and take stable configurations—namely, solute concentration must be high. This requirement is satisfied in austenitic steels containing a large amount of substitutional elements. Furthermore, theoretical calculations have reported that segregation of H decreases the dislocation's line tension and self–energy [114, 115]. The deformation at room temperature and low strain rates, under which H can move coordinatively with dislocations, are therefore favorable for the application of *trough model*. The H–related "stress equivalence" discovered by the authors (Fig. 14(c)) suggests the applicability of such a *trough model* to the H–induced solid solution–hardening. In other words, the conventional thermal activation model in Fig. 11 does not hold for the materials containing a high concentration of alloying elements and diffusible solute H. Instead, the bow–out process of dislocations from troughs, as depicted in Fig. 15, may govern thermal activation parameters.

On the other hand, while the *trough model* is discussed here as a mechanism independent of *solute drag*, when we deal with H, it is still unclear what atomic–scale process actually governs the escape of dislocation from the trough. At first glance, under deformation conditions where the entire H atmosphere can follow the dislocation by maintaining its equilibrium distribution, it seems that the trough itself would also freely move together with the dislocation—that is, dislocation glide resistance is zero. However, the actual situation is not so.

3.2.6 *Diffusion–controlled glide* of dislocation core

The coordinative motion of solute atmosphere with dislocation is driven by the drift flow of solutes. This drift flow stems from the gradient of solute–dislocation interaction energy and solute chemical potential within the dislocation's stress/strain field [37, 52]. In contrast, at the center of the dislocation line, direct interactions between solutes and the dislocation core are of primary importance rather than the behavior of the whole solute atmosphere [37, 52]. Figure 16 illustrates such a situation according to the model drawn by Friedel [116]. Similar to those constituting the surrounding atmosphere, local solutes in the dislocation core also tend to follow the dislocation's movement. However, in doing so, they must undergo one–atomic diffusion jump in the direction of dislocation motion. Given the activation energy for this diffusion jump as W, the dislocation velocity, v_d, under an effective stress, τ^*, can be expressed by an Arrhenius–type rate equation analogous to eq. (9) [52].

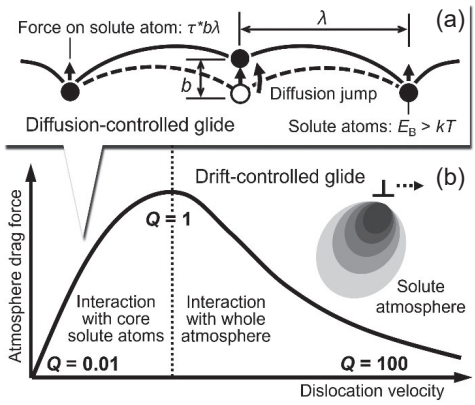

Fig. 16 Description of diffusion- and drift-controlled glide mechanisms and their correspondence with dislocation velocity [37, 116]. The two mechanisms switch each other around the $Q \approx 1$ limit.

$$v_d = \frac{1}{2} v_D \frac{b^2}{\lambda} \left\{ \exp\left(- \frac{W - \tau^* b^2 \lambda}{kT} \right) \right\} \qquad (15)$$

Here, v_D is the Debye frequency, λ is the average interspacing of solutes aligned along the dislocation core, and $W - \tau^* b^2 \lambda$ term corresponds to the thermally supplied energy, ΔG. According to the textbooks of Anderson, Hirth, and Lothe [37], as well as of Caillard and Martin [52], the condition under which this diffusion barrier, W, predominantly resists dislocation motion is as follows—when v_d is smaller than the critical velocity for the maximum atmosphere drag force (*i.e.*, $Q = 1$ in eq. (5)), and when solute–core binding energy, E_B, is greater than thermal vibration energy of the crystal, kT (Fig. 16). Considering that $E_B = 10$–15 kJ/mol (0.1–0.16 eV) in austenitic steels [49, 117, 118], the deformation conditions discussed here (room temperature: $kT = 0.026$ eV) precisely correspond to such a case.

Figure 17 shows the authors' model illustrating the dislocation bow–out from a row of H (*i.e.*, trough) [39]. Similar to the situation shown in Fig. 16, a dislocation line decorated with H advances by generating a bulge, accompanied by diffusion jumps of H atoms to follow the dislocation core. The significance of the diffusion barrier and the size of the bulge then govern the thermally activated process of dislocation motion and the corresponding activation volume. The modification from Friedel's original model lies in the definition of λ in eq. (15), where each bulge assumably involve simultaneous diffusion jumps of multiple H. This assumption is based on two considerations: first, the measured activation volume, V, is much larger than the one predicted from the mean interspacing of H atoms under the

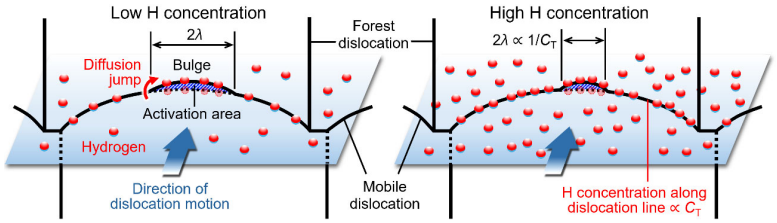

Fig. 17 Schematic drawings of dislocation motion *via* short bulge nucleation by collective thermally activated diffusion jump of multiple hydrogen atoms segregated along the dislocation core: Low hydrogen concentration (left); and high hydrogen concentration (right) [39]. (online color)

present concentration range (Section 3.2.4); second, when H segregation into the dislocation core is considered, H–H spacing along the core becomes even narrower. According to eq. (15), the effective stress, τ^*, acting on the dislocation line assists H–diffusion jumps through the energy term, $W - \tau^* b^2 \lambda$. Let us assume now that the number of H atoms undergoing jumps within a given time period is statistically constant. If so, as the total H concentration increases and the H atoms aligned along the core become denser, the region feasible for such collective H jumps will probabilistically be confined to shorter dislocation segments. This corresponds to a decrease in λ, meaning that the force exerted by the dislocation line on individual H atoms (Fig. 16(a)) becomes smaller. Consequently, in order to maintain $W - \tau^* b^2 \lambda$ constant so that the dislocation can move at a rate consistent with the applied strain rate, τ^* must be increased. As a result, solid solution–hardening occurs through the increase in effective stress. This hypothesis is quite simplified. Nevertheless, it qualitatively explains the involvement of thermally activated processes in H–induced solid solution–hardening, the reduction of V (increase in S), and their dependence on H concentration.

To incorporate the H concentration–dependence of solid solution–hardening and activation volume to the model in Fig. 17, one can refer quantitatively to how the local H concentration near the dislocation core is correlated with the average H concentration throughout the material. When segregation sites such as dislocations coexist with interstitial lattice sites (Fig. 2), the equilibrium H concentration, C_T, at the segregation sites under an average H concentration, C_0, follows the Fermi–Dirac statistics [119].

$$\frac{C_T}{1 - C_T} = \frac{C_0}{1 - C_0} \exp\left(\frac{E_B}{RT}\right) \tag{16}$$

Figure 18 shows the relationship between C_0 and C_T as a function of temperature, calculated using eq. (16). Here, the H–dislocation binding energy in austenitic steel, $E_B \approx 13$ kJ/mol, obtained by Atrens *et al.* [117] *via* internal friction measurements, was employed. The C_T increases sharply with decreasing temperature, then tends to saturate. Notably, in the regime around room temperature, the influence of C_0 on C_T is most pronounced. The inset in Fig. 18 extracts the C_0–C_T relationship at room temperature (300 K). Within the H concentration of 2000–8000 at ppm (*i.e.*, the range targeted by the authors), C_T is approximately proportional to C_0, as fitted by the dashed line.

According to the model in Fig. 17, if the number of H atoms within the bulge (*i.e.*, those capable of jumping within

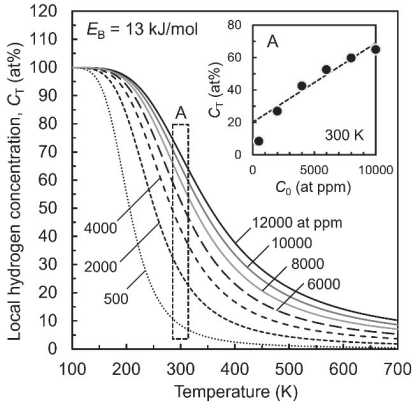

Fig. 18 Temperature-dependence of the local hydrogen concentration along dislocation lines, C_T, in austenitic steel estimated from eq. (16). The inset shows the relationship between average hydrogen concentration in the material, C_0, and C_T at room temperature.

a given time) is statistically constant, the bulge length λ becomes inversely proportional to the H concentration C_T along the dislocation core. Therefore, given that the forward displacement of the bulge during thermal activation is sufficiently smaller than λ, the activation volume V becomes inversely proportional to both C_T and C_0. This aligns with the experimental observation in Fig. 14(b), where S is proportional to C_0. Similarly, if $\lambda \propto 1/C_0$ in eq. (15), then under a given deformation rate where $W - \tau^* b^2 \lambda$ is constant, the effective stress τ^* becomes proportional to C_0 (inversely proportional to V). Although this is a simple approximation, it reasonably explains the characteristics of H–induced solid solution–hardening—namely, that the magnitude of strengthening is proportional to the average H concentration (Fig. 1)—when considered together with the H concentration–dependence of *solute drag* force. Note that in eq. (15), the thermal energy $W - \tau^* b^2 \lambda$ decreases as a linear function of stress. Substituting such a relation into eq. (7) ($\Delta G = \Delta G_0 - \tau^* V$) yields a constant V for a given λ, indicating that the energy barrier resisting dislocation motion has a rectangular potential profile. In practice, however, the obstacle profile usually possesses a finite slope (Fig. 11(c)). Thus, V also becomes a stress–dependent parameter. The stress–dependence of thermal energy in real obstacle profiles can be generalized using two constants, $0 < p < 1$ and $1 < q < 2$, together with the effective stress at 0 K, $\hat{\tau}$ (the peak stress in Fig. 11(c)), as follows [52, 92].

$$\Delta G = \Delta G_0 \left\{ 1 - \left(\frac{\tau^*}{\hat{\tau}} \right)^p \right\}^q \tag{17}$$

Deriving the specific values of p and q in eq. (17), as well as measuring the stress–dependence of activation volume, are among the tasks that the authors should initiatively deal with. Such efforts will enable us to further elaborate on the diffusion–jump process of H within the dislocation core.

Although the commercial alloy used by the authors contained dilute H (∼300 at ppm) even in the non–charged condition, this concentration is far lower than the regime that fits the linear approximation in the inset of Fig. 18. In this case, the H along the dislocation line no longer serves as the predominant factor for λ. Consequently, denser elements such as Cr and Ni may govern the "stress equivalence" of activation volume (Fig. 14(c)). In contrast, as can also be inferred from Fig. 18, when C_0 exceeds 10000 at ppm, and H becomes highly concentrated throughout the material, C_T tends to saturate even at room temperature. Figure 18 thus suggests that, in the high H concentration regime, the proportionality between H–induced solid solution–hardening and H concentration no longer holds. Indeed, in the experiments by Abraham and Altstetter (Section 2.1) [33], such a tendency of saturation has been observed.

3.3 Roles of randomly dispersed H and H–Cr complexes

Under deformation conditions where H can follow dislocation movement, the local H concentration around dislocations is overwhelmingly higher than the average H concentration (Fig. 18). Therefore, the contribution of H atoms randomly dispersed in the matrix is of limited importance to the dislocation's glide resistance. However, under relatively high strain rate or at low temperatures where H diffusion becomes infeasible, dispersed H may also play a significant role. Referring to Figs. 3 and 8 again, a considerable solid solution–hardening indeed appears even under temperatures and strain rates corresponding to $Q > 100$ in Fig. 7. This indicates that dislocations experience some resistance when passing near H atoms occupying interstitial lattice sites. We stated in Section 2.1 that lattice strain caused by H alone cannot account for the observed solid solution–hardening. As an alternative factor, we have focused on the electrochemical affinity between H and Cr atoms, as shown in Fig. 6. The same reasoning applies to carbon and nitrogen: there exists an attractive interaction between Cr and these three types of interstitial elements. For carbon, a binding energy of approximately 0.1 eV has been reported; for nitrogen, it is about 0.2 eV [120]. If the decrease in H–absorption energy resulting from Cr substitution—compared to an O–site surrounded solely by Fe atoms—in Fig. 6 is equal to the H–Cr binding energy (*e.g.*, 0.05–0.10 eV for one or two Cr atoms), its magnitude is comparable to that of carbon or nitrogen.

When interstitial and substitutional solutes form complexes (*i–s* complexes) on the slip plane, extra energy is required for dislocation movement, as the motion passing through these *i–s* complexes necessitates their collapse. The dislocations consequently experience some glide resistance. Shibata *et al.* conducted strain–controlled low–cycle fatigue tests of Fe–20Cr–15Ni– and Fe–15Cr–15Ni–based austenitic steels, to which ≈0.3 mass% carbon was added, measuring the flow stress fluctuation during cyclic loading [45]. They demonstrated that carbon promotes cyclic softening, changing dislocation structures from cellular to planar configuration. Their findings were ascribed to the dissolution of *i–s* complexes *via* the shuttling motion of dislocations and the consequent glide plane softening. Similar results have also been reported for nitrogen–added steel [46]. These provide strong experimental evidence supporting the contribution of *i–s* complexes to solid solution–hardening.

Although H–diffusion becomes slower at low temperatures, H atoms are still capable of jumping on a relatively short time scale of ≈100 s even at temperatures as low as 200 K (Fig. 4(b)). This is markedly different from the behavior of carbon and nitrogen. To say, even if an *i–s* complex comprising H is dissolved by dislocation motion, it can be readily repaired through subsequent diffusion jumps of H. The repetition of such processes, which are not anticipated for carbon and nitrogen, may play a significant role in strengthening, particularly in the later stages of deformation. As insistently mentioned, H–induced lattice strain alone cannot account for the observed solid solution–hardening. However, as suggested by the Snoek–type internal friction peak [68, 70], the *i–s* complexes can be associated with anisotropic tetragonal distortion. Unlike isotropic lattice expansion interacting only with edge dislocations, tetragonal distortion strongly interacts with screw dislocations as well [37], potentially contributing to solid solution–hardening. Moreover, the attractive H–Cr interaction is of particular interest for advancing and quantifying the *diffusion–controlled glide* model in Fig. 17. If H–Cr pairing occurs within the dislocation core, larger energy would be required for the diffusion jump of H to be decoupled from Cr under a given applied stress. This may be one of the reasons for the correlation between Cr content and H–induced solid solution–hardening in Fig. 5. Further elucidation of H–Cr interactions are thus highly desired, as they likely play fundamental roles in the strengthening by both segregated and randomly dispersed H.

Referring to Fig. 3(c) again, in the regime below 200 K where H diffusion becomes essentially infeasible, the magnitude of H–induced solid solution–hardening is completely independent of strain rate, in contrast to the behavior at room temperature. This fact cannot be explained by considering only the presence of H as individual dispersed atoms or as H–Cr pairs. One has to consider the possible contribution of long–range obstacles that could transform the strengthening mechanism into an athermal process—for instance, short–range ordered structures of H–Cr pairs in regions where Cr is stochastically enriched. A systematic collection of experimental data will be essential to clarify this possibility.

4. Macroscopic Picture and Rate–Controlling Process of Thermally Activated Deformation under the Presence of H

4.1 Modelling deformation behavior by spring–damper system

In this section, from a macroscopic perspective, the augmented stress relaxation *via* H–induced solid solution–hardening (Fig. 12(a)) and related phenomena are discussed based on the nature of H as a thermally activatable obstacle.

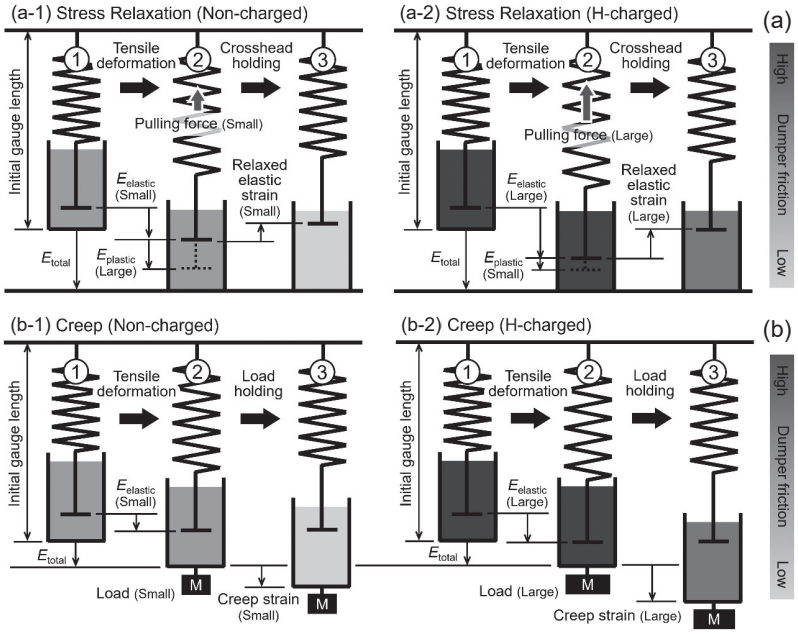

Fig. 19 Spring-dumper representations of (a) stress relaxation (constant strain) and (b) creep (constant stress) deformation in elasto-plastic solids. (a-1) and (b-1) represent non-charged state where frictional coefficient of dumper is small, while (a-2) and (b-2) denote H-charged condition with large dumper friction owing to solute hydrogen atoms working as thermal obstacles.

The plastic deformation wherein flow stress contains its time–dependent component can be modeled as a viscoelastic system consisting of a spring and damper (Fig. 19). The displacements of the spring and damper represent the elastic deformation ($E_{elastic}$) and plastic deformation ($E_{plastic}$), respectively. The frictional resistance within the damper, which depends on deformation rate, corresponds to the effective stress required for thermally activated dislocation motion. In a stress relaxation test, the machine crosshead is arrested after a given amount of deformation. Then, the stress reduction is recorded as a function of time. This operation corresponds to the illustration in Fig. 19(a-1): under a constant total strain (E_{total}), the gradual contraction of the spring (a decrease in elastic strain) is replaced by the displacement in the damper (an increase in plastic strain), as represented by stages ②–③ in Fig. 19(a-1).

The involvement of H as short–range (thermal) obstacles can be represented as an increase in the frictional coefficient of the damper—the proportionality constant linking the frictional resistance with the deformation rate (Fig. 19(a-2)). The variation of such frictional resistance is illustrated by the gradient shading on the right side of Fig. 19(a-2). When a total strain, E_{total}, is applied at a given strain rate, the greater frictional coefficient in the H–charged specimen temporarily makes the spring deformation, $E_{elastic}$, larger and the damper deformation, $E_{plastic}$, smaller (Fig. 19(a-2) ②). A greater $E_{elastic}$ implies that the specimen is subjected to a higher load—emergence of H–induced solid solution–hardening (Fig. 19(a-2) ②). A key point here is the experimentally observed increase in strain rate sensitivity, S, in the H–charged specimen (Fig. 14), which is physically equivalent to an increase in frictional coefficient in the damper. This indicates that the H–charged specimen exhibits a greater change in frictional resistance when the deformation rate is changed by a given magnitude. Consequently, upon halting the crosshead, the slowing down of the deformation rate leads to a more rapid decrease in frictional resistance. Driven by the stronger pulling force due to a larger $E_{elastic}$, a more pronounced spring contraction then occurs (Fig. 19(a-2) ③). The augmented stress relaxation in Fig. 12(a) virtually reflects such a process.

The authors reproduced a similar process through room–temperature creep tests on H–charged Type310S steel [91]. Unlike stress relaxation with a constant total strain, plastic deformation proceeds under a constant load in the case of creep. This operation corresponds to the illustration in Fig. 19(b-1)—a given total strain is first applied, followed by a load–holding. During the load–holding period, the spring part remains fixed, while only the damper part continues to deform with time. Until applying the same total strain to both non–charged and H–charged specimens (Fig. 19(b-2)), the process is essentially identical to the previous case shown in Fig. 19(a). However, once the load–holding starts, both the spring deformation (*i.e.*, applied load) and the decreasing rate of the damper's frictional resistance are greater in the H–charged specimen than those in the non–charged specimen—just as in the stress relaxation case. Considering these higher applied load and lower frictional resistance in the H–charged specimen, one can expect a faster creep rate.

Figures 20(a) and (b) show the stress–strain curve and the corresponding creep curve in the tests wherein the specimen was first deformed at a constant strain rate, followed by load–holding. As predicted from Fig. 19(b), when the load was held at the same total strain, the amount of creep during the holding period was clearly larger in the H–charged specimen. In contrast, Figs. 20(c) and (d) present the creep behavior of the H–charged specimen when the load was immediately reduced to match the level in the non–charged specimen before holding. In terms of Fig. 19(b), this procedure

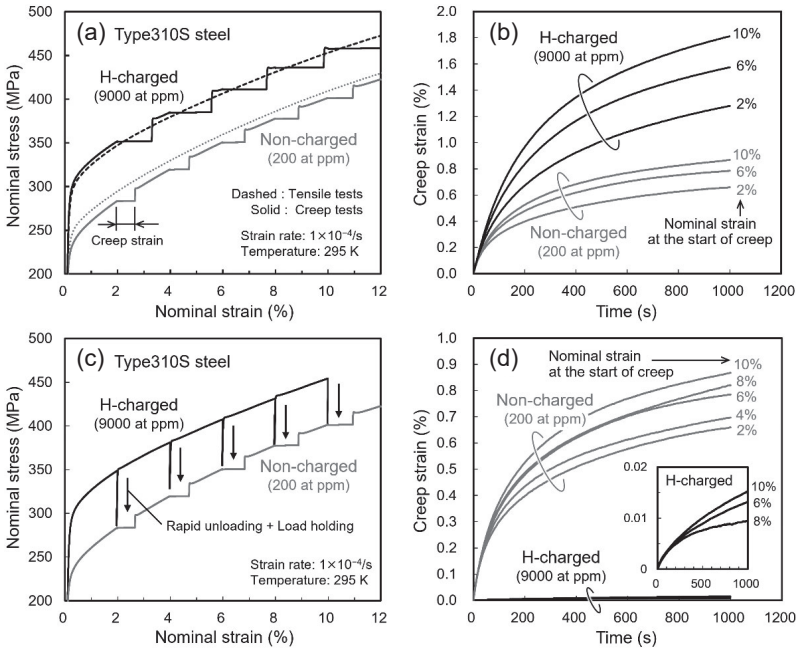

Fig. 20 Room temperature creep behavior of non-charged and hydrogen-charged Type310S austenitic steel [91]. In (a) and (b), 1000 s load holdings were implemented during normal tensile tests, while hydrogen-charged specimen was unloaded to the same flow stress level with the non-charged specimen before load holding in (c) and (d). The inset in (d) magnifies the creep curves in H-charged specimen.

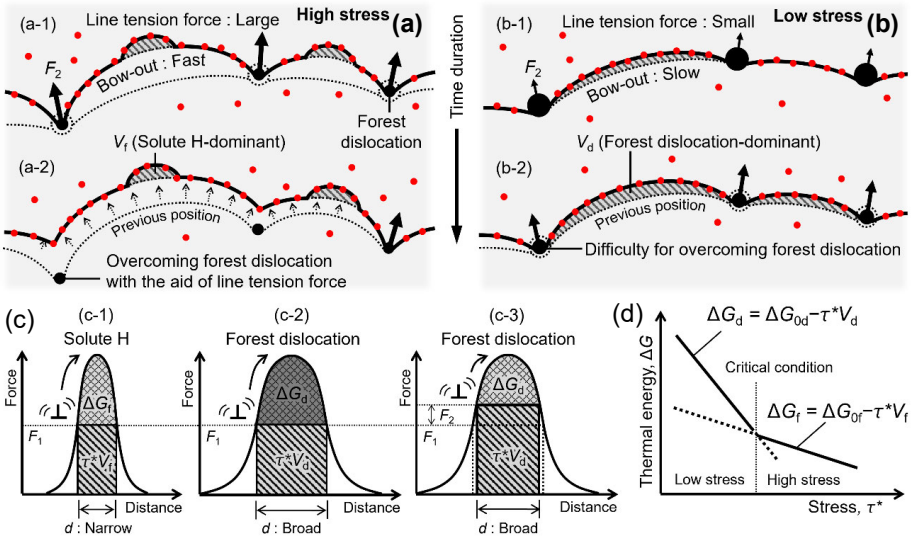

Fig. 21 Schematic illustration of the stress-dependent change of rate-controlled obstacles for thermally activated plastic flow in the presence of solute H [91]. Mobile dislocation can successively overcome H and forest dislocations at (a) high stress, while surmounting the latter obstacle type becomes difficult at (b) low stress due to the glide resistance against dislocation by H. (c) and (d) represent the stress-dependence of ΔG in the obstacle profiles with different width. (online color)

corresponds to inserting an additional step between stages ② and ③—the spring deformation is restored to the same level as that in the non–charged specimen. Under such conditions, even at stress levels where pronounced creep is observed in the non–charged specimen, the creep in the H–charged specimen is suppressed dramatically. This suppression of creep under an identical load indicates an increase in damper's frictional coefficient assumed in Fig. 19.

4.2 Stress–dependence of rate–controlling factors

It is worth envisaging that how the series of H–effects on stress relaxation and creep can be represented in the model context in Fig. 17. Figure 21 reproduces the model by viewing it from above the slip plane. In general, junctions with forest dislocations act as relatively strong and extended obstacles [92, 96, 121]. Therefore, a moving dislocation may bow–out between these strong pinning points *via* successively overcoming weaker, more localized, and closely spaced obstacles—namely, H atoms—by thermal activation (Fig. 21(a-1)). Let us reconsider the physical sense of obstacle width in thermal activation. When the same force, F_1, acts on both forest dislocation and H atom from a

dislocation line, the thermal energy, ΔG, required to overcome these obstacles is inevitably larger for a more extended obstacle—forest dislocation (ΔG_d)—than for H atom (ΔG_f) (Figs. 21(c-1) and (c-2)). Consequently, under a given applied stress, the frequency of which a dislocation surmounts H atoms is overwhelmingly higher than that for forest dislocations. To shorten the time required for overcoming a forest dislocation to the same level as for H, an extra force, F_2, must be supplied (Fig. 21(c-3)), so as to reduce ΔG_d until $\Delta G_d = \Delta G_f$. F_2 is provided by the line tension force acting on the forest dislocations from the bowing–out segment of the moving dislocation line (Fig. 21(a-1)). As time progresses, the bow–out segment decreases its radius of curvature. Once the curvature and line tension force reach a critical level, the mobile dislocation overcomes forest dislocation and exhibits long–range motion. Figure 21(d) illustrates such competition between obstacle types in terms of the stress–dependence of ΔG. If activation energies at $\tau^* = 0$ for forest dislocation and H are denoted as ΔG_{0d} and ΔG_{0f}, then assuming $\Delta G_d > \Delta G_f$ and $V_d > V_f$ (for simplicity, both obstacles are assumed to have rectangular potential profiles), the stress dependence of ΔG_d and ΔG_f can be expressed as two straight lines. The intersection between these two lines corresponds to $\Delta G_d = \Delta G_f$. A similar schematic diagram was first proposed by Schoeck [122], and later demonstrated in computational simulations on solid–solution alloys by Curtin and co–workers [121].

As is evident from Fig. 21(d), the deformation kinetics under high–stress (above the "Critical condition" in Fig. 21(d)) is solely governed by ΔG_f, while a smaller barrier ΔG_d no longer serves as the rate–controlling factor. Consequently, the experimentally measurable activation parameters are also dominated by ΔG_f. The ΔG_f–governed domain expands with increasing difference between V_d and V_f—that is, with increasing H concentration. This accounts well for the experimental trend in the *Haasen plot* (Fig. 14(a)), where the contribution of forest dislocation to S becomes less apparent (*i.e.*, the slope decreases) as the H concentration increases. Meanwhile, as the applied stress decreases and ΔG_f increases (Fig. 21(c-1)), the dislocation motion *via* overcoming H atoms may sharply slow down. This slowdown not only affects the dislocation segments confined between forest junctions. Rather, it also lowers the rate at which forest dislocations are surmounted, through a decrease in the line tension force acting on the mobile–forest junctions. In other words, under low–stress, the rate–controlling process shifts to the stage where mobile dislocations dragging H to overcome forest junctions. The suppression of creep at low stresses in H–charged specimens (Figs. 20(c) and (d)) can thus be rationalized on this basis.

5. Summary and Future Perspectives

In Fe–Cr–Ni austenitic steels, interstitial H produces solid solution–hardening comparable to that achieved by carbon or nitrogen. In the present paper, the phenomenology of such H–induced solid solution–hardening was addressed, reviewing the principal experimental findings reported to date—namely, that (i) the strengthening exhibits its peak at specific temperature and strain rate, (ii) it is linearly proportional to H concentration, and (iii) it strongly depends on Cr content in the alloy. Based on the state and diffusivity of H within the material, the underlying mechanisms governing H–induced solid solution–hardening were discussed in terms of three essential factors:

1). *Solute drag* of H atmosphere surrounding dislocations (Section 3.1)
2). *Diffusion–controlled glide* of dislocation core with H (Section 3.2)
3). Resistance from randomly dispersed H and *i–s* complexes (Section 3.3)

Although some discussions remain qualitative, we believe that the combination and interplay of these three factors can collectively account for the phenomenological characteristics of H–induced solid solution–hardening, the changes in thermally activated deformation behavior, and the "stress equivalence" upon H–addition.

Figure 22 summarizes the contributions of these factors 1)–3) to solid solution–hardening on a temperature–strain rate map, assuming a mobile dislocation density corresponding to the vicinity of yield stress ($\rho_m = \sim 10^{12}/m^2$). The gradient shading in the map indicates that, when the responsible factors are associated with H segregated at dislocations, the local H concentration should decrease at elevated temperatures (Fig. 18), leading to a reduced strengthening capability. In addition, when the obstacles are thermally activatable in nature, dislocations can more easily overcome them at higher temperatures and lower strain rates, further diminishing the strengthening. H–induced solid solution–hardening manifests most effectively when synergistic contributions from 1)–3) reach their maximum. According to the authors' experiments, this optimal condition corresponds to deformation at around 300 K and strain rates on the order of 10^{-5}–10^{-4}/s.

The dashed lines in Fig. 22 delineate the temperature and strain rate ranges experimentally verified in this study, which, however, represent only a small fraction of the overall parameter space. Expanding coverage into the unexplored regions is essential for reinforcing and refining the present

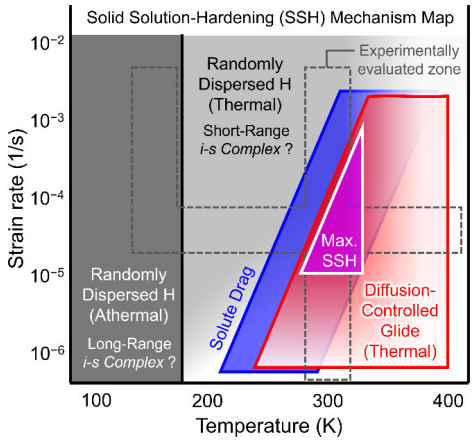

Fig. 22 Temperature- and strain rate-dependent changes and synergies of the mechanisms responsible for hydrogen-induced solid solution-hardening in Fe-Cr-Ni austenitic steels at their yield stress. The fade-out of filling color denotes the weakening contribution of each mechanism. (online color)

framework. In particular, systematic data acquisition below 200 K—where H diffusivity drops sharply—will be crucial for clarifying the role of *i–s* complexes, the most uncertain aspect at present. During post–yield deformation at room temperature, where the mobile dislocation density increases rapidly, and the *solute drag* regime in Fig. 22 shifts toward higher strain rates, *diffusion–controlled glide* is expected to dominate. Although the current modeling reproduces the observed behavior reasonably well, the atomic–scale mechanisms—especially H transport within dislocation cores and the role of alloying elements—remain unresolved. Future progress will require quantitative experiments linking the activation parameters of dislocation motion and H diffusion, the interaction energies between H and substitutional atoms, and the potential profile of H as a short–range obstacle. Complementary computational approaches, such as molecular dynamics simulations, will likewise be indispensable. Moreover, effects unique to FCC alloys (*e.g.*, dislocation dissociation into partials) and deformation–induced defects (*e.g.*, vacancies) are also expected to play a key role. These concerted efforts—including the authors' forthcoming work—are anticipated to advance a more comprehensive understanding of H–induced solid solution–hardening.

Acknowledgements

The series of research presented in this paper was supported by JSPS KAKENHI (Nos. 21K14045 and 24K17180), the JFE 21st Century Foundation, the Iwatani Naoji Foundation, and the Yoshida–Gakujutu Foundation. The authors would like to express their sincere gratitude to Prof. Masaki Tanaka and Prof. Emeritus Kenji Higashida of Kyushu University for their valuable advice and insightful discussions on the topics presented in Section 3.2.

Open Access

This paper is open access and licensed under a CC-BY-NC-ND license. You are free to share or adapt the materials as long as you follow the license term: Attribution, NonCommercial, and NoDerivatives. To view a copy of this license, visit https://creativecommons.org/licenses/by-nc-nd/4.0/.

REFERENCES

[1] R.P. Gangloff and B.P. Somerday: *Gaseous Hydrogen Embrittlement of Materials in Energy Technologies: The Problem, its Characterisation and Effects on Particular Alloy Classes*, (Woodhead Publishing, 2012).

[2] M. Nagumo: *Fundamentals of Hydrogen Embrittlement*, 2nd ed., (Springer, 2023).

[3] L. Zhang, M. Wen, M. Imade, S. Fukuyama and K. Yokogawa: Effect of nickel equivalent on hydrogen gas embrittlement of austenitic stainless steels based on type 316 at low temperatures, Acta Mater. **56** (2008) 3414–3421.

[4] G. Han, J. He, S. Fukuyama and K. Yokogawa: Effect of strain-induced martensite on hydrogen environment embrittlement of sensitized austenitic stainless steels at low temperatures, Acta Mater. **46** (1998) 4559–4570.

[5] M. Koyama, T. Ogawa, D. Yan, Y. Matsumoto, C.C. Tasan, K. Takai and K. Tsuzaki: Hydrogen desorption and cracking associated with martensitic transformation in Fe-Cr-Ni-Based austenitic steels with different carbon contents, Int. J. Hydrogen Energy **42** (2017) 26423–26435.

[6] T. Kanezaki, C. Narazaki, Y. Mine, S. Matsuoka and Y. Murakami: Effects of hydrogen on fatigue crack growth behavior of austenitic stainless steels, Int. J. Hydrogen Energy **33** (2008) 2604–2619.

[7] M. Koyama, S. Okazaki, T. Sawaguchi and K. Tsuzaki: Hydrogen Embrittlement Susceptibility of Fe-Mn Binary Alloys with High Mn Content: Effects of Stable and Metastable ε-Martensite, and Mn Concentration, Metall. Mater. Trans. A **47** (2016) 2656–2673.

[8] J. Yamabe, O. Takakuwa, H. Matsunaga, H. Itoga and S. Matsuoka: Hydrogen diffusivity and tensile-ductility loss of solution-treated austenitic stainless steels with external and internal hydrogen, Int. J. Hydrogen Energy **42** (2017) 13289–13299.

[9] T. Omura, H. Hirata, M. Miyahara and T. Kudo: Effect of chemical compositions on embrittlement properties of stainless steels in highly pressurized gaseous hydrogen environments, Zairyo to Kankyo **57** (2008) 30–36.

[10] S. Takaki, S. Nanba, K. Imakawa, A. Macadre, J. Yamabe, H. Matsunaga and S. Matsuoka: Determination of hydrogen compatibility for solution-treated austenitic stainless steels based on a newly proposed nickel-equivalent equation, Int. J. Hydrogen Energy **41** (2016) 15095–15100.

[11] B.-H. Chi, T. Nakazawa and K. Shibata: Effects of alloying elements on hardening and restoration behavior of 15Cr-15Ni high hardness non-magnetic stainless steel, ISIJ Int. **30** (1990) 615–624.

[12] K. Oda, N. Kondo and K. Shibata: X-ray absorption fine structure analysis of interstitial (C, N)-substitutional (Cr) complexes in austenitic stainless steels, ISIJ Int. **30** (1990) 625–631.

[13] N. Ohkubo, K. Miyakusu, Y. Uematsu and H. Kimura: Effect of Alloying Elements on the Mechanical Properties of the Stable Austenitic Stainless Steel, ISIJ Int. **34** (1994) 764–772.

[14] M.L.G. Byrnes, M. Grujicic and W.S. Owen: Nitrogen strengthening of a stable austenitic stainless steel, Acta Metall. **35** (1987) 1853–1862.

[15] E. Werner: Solid solution and grain size hardening of nitrogen-alloyed austenitic steels, Mater. Sci. Eng. A **101** (1988) 93–98.

[16] A.W. Thompson and J.A. Brooks: The mechanism of precipitation strengthening in an iron-base superalloy, Acta Metall. **30** (1982) 2197–2203.

[17] T. Hosoda, Y. Ogawa, O. Takakuwa, S. Motomura, H. Hosoi and H. Matsunaga: Effects of Ni Concentration and Aging Heat Treatment on the Hydrogen Embrittlement Behavior of Precipitation-Hardened High-Mn Austenitic Steel, Tetsu-to-Hagané **108** (2022) 156–172.

[18] S. Takaki, S. Tanimoto, K. Tomimura and Y. Tokunaga: Strengthening of Metastable 16–10 Austenitic Stainless Steel by Ultra Grain Refining, Tetsu-to-Hagané **74** (1988) 1058–1064.

[19] R. Ke, C. Hu, M. Zhong, X. Wan and K. Wu: Grain refinement strengthening mechanism of an austenitic stainless steel: critically analyze the impacts of grain interior and grain boundary, J. Mater. Res. Technol. **17** (2022) 2999–3012.

[20] S. Takaki: Strengthening Mechanisms and Ultimate Strength of Iron, Materia Japan **36** (1997) 675–679.

[21] K. Wada, J. Yamabe, Y. Ogawa, O. Takakuwa, T. Iijima and H. Matsunaga: Comparative study of hydrogen-induced intergranular fracture behavior in Ni and Cu–Ni alloy at ambient and cryogenic temperatures, Mater. Sci. Eng. A **766** (2019) 138349.

[22] K. Ichii, M. Koyama, C.C. Tasan and K. Tsuzaki: Comparative study of hydrogen embrittlement in stable and metastable high-entropy alloys, Scr. Mater. **150** (2018) 74–77.

[23] Y. Ogawa, H. Hosoi, K. Tsuzaki, T. Redarce, O. Takakuwa and H. Matsunaga: Hydrogen, as an alloying element, enables a greater strength-ductility balance in an Fe-Cr-Ni-based, stable austenitic stainless steel, Acta Mater. **199** (2020) 181–192.

[24] H. Nishida, Y. Ogawa and K. Tsuzaki: Chemical composition dependence of the strength and ductility enhancement by solute hydrogen in Fe–Cr–Ni-based austenitic alloys, Mater. Sci. Eng. A **836** (2022) 142681.

[25] Y. Ogawa: Temperature-sensitive ductilization in hydrogen-alloyed Fe-Cr-Ni austenitic steel by enhanced deformation twinning, Scr. Mater. **238** (2024) 115760.

[26] Y. Murakami, T. Kanezaki and Y. Mine: Hydrogen Effect against Hydrogen Embrittlement, Metall. Mater. Trans. A **41** (2010) 2548–

2562.
[27] T. Boniszewski and G.C. Smith: The influence of hydrogen on the plastic deformation ductility, and fracture of nickel in tension, Acta Metall. **11** (1963) 165–178.
[28] S.K. Lawrence, Y. Yagodzinskyy, H. Hänninen, E. Korhonen, F. Tuomisto, Z.D. Harris and B.P. Somerday: Effects of grain size and deformation temperature on hydrogen-enhanced vacancy formation in Ni alloys, Acta Mater. **128** (2017) 218–226.
[29] J.S. Blakemore: The Portevin-Le Chatelier Effect in hydrogenated nickel, Metall. Trans. **1** (1970) 145–149.
[30] J.S. Blakemore: The portevin-le chatelier effect in hydrogenated nickel alloys, Metall. Trans. **1** (1970) 151–156.
[31] K. Wada and J. Yamabe: The effect of the Ni/Cu ratio on H-induced ductility loss and its mechanism in Cu–Ni binary alloy system, Int. J. Hydrogen Energy **46** (2021) 39577–39589.
[32] O. Takakuwa, Y. Mano and H. Soyama: Increase in the local yield stress near surface of austenitic stainless steel due to invasion by hydrogen, Int. J. Hydrogen Energy **39** (2014) 6095–6103.
[33] D.P. Abraham and C.J. Altstetter: The effect of hydrogen on the yield and flow stress of an austenitic stainless steel, Metall. Mater. Trans. A **26** (1995) 2849–2858.
[34] C. Sanmarchi: Effects of alloy composition and strain hardening on tensile fracture of hydrogen-precharged type 316 stainless steels, Int. J. Hydrogen Energy **33** (2008) 889–904.
[35] M. Koyama, K. Ichii and K. Tsuzaki: Strain Rate and Temperature Effects on Hydrogen Embrittlement of Stable and Metastable High-Entropy Alloys, Phys. Mesomech. **25** (2022) 385–392.
[36] D. Hull and D.J. Bacon: *Introduction to Dislocations*, 3rd ed., (Butterworth-Heinemann, 2011) https://doi.org/10.1016/C2009-0-64358-0.
[37] P.M. Anderson, J.P. Hirth and J. Lothe: *Theory of Dislocations*, 3rd ed., (Cambridge University Press, 2017).
[38] Y. Ogawa, O. Takakuwa and K. Tsuzaki: Solid-solution hardening by hydrogen in Fe–Cr–Ni-based austenitic steel: Temperature and strain rate effects, Mater. Sci. Eng. A **879** (2023) 145281.
[39] Y. Ogawa, M. Tanaka, T. Fujita and A. Shibata: Thermally activated dislocation motion in hydrogen-alloyed Fe–Cr–Ni austenitic steel revisited via Haasen plot, Int. J. Hydrogen Energy **74** (2024) 170–182.
[40] Y. Ogawa and T. Fujita: Solid solution-hardening by hydrogen in Fe–Cr–Ni-based austenitic steel studied by strain rate sensitivity measurement: Contributions of effective stress and solute drag, Mater. Sci. Eng. A **911** (2024) 146941.
[41] J. Moriyama, O. Takakuwa, M. Yamaguchi, Y. Ogawa and K. Tsuzaki: The contribution of Cr and Ni to hydrogen absorption energy in Fe-Cr-Ni austenitic systems: A first-principles study, Comput. Mater. Sci. **232** (2024) 112650.
[42] J.C. Slater: Atomic Radii in Crystals, J. Chem. Phys. **41** (1964) 3199–3204.
[43] H.M. Ledbetter and M.W. Austin: Dilation of an fcc Fe–Cr–Ni alloy by interstitial carbon and nitrogen, Mater. Sci. Technol. **3** (1987) 101–104.
[44] P. Marshall: *Austenitic Stainless Steels: Microstructure and Mechanical Properties*, (Springer, 1984).
[45] K. Shibata, M. Kogita, C.-S. Chen and T. Fujita: Effects of Carbon and Silicon on Softening in Low-cycle Fatigue of Austenitic Stainless Steels, Trans. Iron Steel Inst. Jpn. **28** (1988) 406–412.
[46] K. Shibata, N. Namura, Y. Kishimoto and T. Fujita: Low Cyclic Fatigue Softening of Austenitic Stainless Steels, Tetsu-to-Hagané **69** (1983) 2076–2083.
[47] T. Ito, Y. Ogawa, W. Gong, W. Mao, T. Kawasaki, K. Okada, A. Shibata and S. Harjo: Role of solute hydrogen on mechanical property enhancement in Fe–24Cr–19Ni austenitic steel: An in situ neutron diffraction study, Acta Mater. **287** (2025) 120767.
[48] D.G. Ulmer and C.J. Altstetter: Phase relations in the hydrogen-austenite system, Acta Metall. Mater. **41** (1993) 2235–2241.
[49] X.W. Zhou, C. Nowak, R.S. Skelton, M.E. Foster, J.A. Ronevich, C. San Marchi and R.B. Sills: An Fe–Ni–Cr–H interatomic potential and predictions of hydrogen-affected stacking fault energies in austenitic stainless steels, Int. J. Hydrogen Energy **47** (2022) 651–665.
[50] C. San Marchi, T. Michler, K.a. Nibur and B.P. Somerday: On the physical differences between tensile testing of type 304 and 316 austenitic stainless steels with internal hydrogen and in external hydrogen, Int. J. Hydrogen Energy **35** (2010) 9736–9745.
[51] K.J. Irvine, T. Gladman and F.B. Pickering: The strength of austenitic stainless steels, J. Iron Steel Inst. **207** (1969) 1017–1028.
[52] D. Caillard and J.L. Martin: *Thermally Activated Mechanisms in Crystal Plasticity*, 1st ed., (Pergamon, 2003).
[53] A. Van Den Beukel: Theory of the effect of dynamic strain aging on mechanical properties, Phys. Status Solidi A **30** (1975) 197–206.
[54] U.F. Kocks: Kinetics of solution hardening, Metall. Trans. A **16** (1985) 2109–2129.
[55] X. Zhang, R. Takahashi, T. Akiyama and J. Yagi: Carburization Rate into Solid Iron at CO-CO2 Atmosphere, Tetsu-to-Hagané **83** (1997) 299–304.
[56] P. Thibaux, A. Métenier and C. Xhoffer: Carbon Diffusion Measurement in Austenite in the Temperature Range 500 °C to 900 °C, Metall. Mater. Trans. A **38** (2007) 1169–1176.
[57] M.I. Ismail, S.S. Iskander and E.B. Saleh: Carburizing of steels, Surf. Technol. **12** (1981) 341–349.
[58] A. Kühl, D. Bergner, H.-J. Ullrich, M. Schlaubitz and P. Karduck: Investigations of nitrogen diffusion in austenitic CrNi steels, Mikrochim. Acta **107** (1992) 295–302.
[59] R. Hales and A.C. Hill: The diffusion of nitrogen in an austenitic stainless steel, Met. Sci. **11** (1977) 241–244.
[60] J. Hirvonen and A. Anttila: Annealing behavior of implanted nitrogen in AISI 316 stainless steel, Appl. Phys. Lett. **46** (1985) 835–836.
[61] T. Perng and C.J. Altstetter: Effects of deformation on hydrogen permeation in austenitic stainless steels, Acta Metall. **34** (1986) 1771–1781.
[62] Y. Mine and T. Kimoto: Hydrogen uptake in austenitic stainless steels by exposure to gaseous hydrogen and its effect on tensile deformation, Corros. Sci. **53** (2011) 2619–2629.
[63] C. San Marchi, B. Somerday and S. Robinson: Permeability, solubility and diffusivity of hydrogen isotopes in stainless steels at high gas pressures, Int. J. Hydrogen Energy **32** (2007) 100–116.
[64] O. Takakuwa, J. Yamabe, H. Matsunaga, Y. Furuya and S. Matsuoka: Comprehensive Understanding of Ductility Loss Mechanisms in Various Steels with External and Internal Hydrogen, Metall. Mater. Trans. A **48** (2017) 5717–5732.
[65] J. Moriyama, M. Yamaguchi and O. Takakuwa: Effects of antagonistic interaction between Cr and Ni on hydrogen solubility in a Fe-Cr-Ni ternary austenitic system: A first-principles calculation, Mater. Today Commun. **40** (2024) 110059.
[66] K. Hirata, S. Iikubo and H. Ohtani: First-principles Calculations of the Effects of Mn, Cr, and Ni on Hydrogen Diffusion in BCC, FCC, and HCP Fe, Tetsu-to-Hagané **105** (2019) 231–239.
[67] E.J. Song, H.K.D.H. Bhadeshia and D.-W. Suh: Interaction of aluminium with hydrogen in twinning-induced plasticity steel, Scr. Mater. **87** (2014) 9–12.
[68] N. Ide, T. Naito and S. Asano: Internal friction peak in FCC Fe-Cr-Ni alloys hydrogen-charged by gas-equilibration method, Jpn. J. Appl. Phys. **44** (2005) 8088–8090.
[69] S. Asano, R. Tsunoda and R. Otsuka: Internal Friction due to Hydrogen in Austenitic Stainless Steels, J. Japan Inst. Metals **41** (1977) 338–344.
[70] V.G. Gavriljuk, H. Haänninen, S.Y.U. Smouk, A.V. Tarasenko and K. Ullakko: Internal friction in hydrogen-charged CrNi and CrNiMn austenitic stainless steels, Metall. Mater. Trans. A **27** (1996) 1815–1821.
[71] A.H. Cottrell: *Dislocations and Plastic Flow in Crystals*, (Oxford Univ. Press, New York, 1953).
[72] H.K. Birnbaum and P. Sofronis: Hydrogen-enhanced localized plasticity—a mechanism for hydrogen-related fracture, Mater. Sci. Eng. A **176** (1994) 191–202.
[73] M. Kurkela and R.M. Latanision: The effect of plastic deformation on the transport of hydrogen in nickel, Scr. Metall. **13** (1979) 927–932.
[74] R. Matsumoto, S.T. Oyinbo, M. Vijendran and S. Taketomi: Hydrogen Effect on the Mobility of Edge Dislocation in α-Iron: A Long-Timescale Molecular Dynamics Simulation, ISIJ Int. **62** (2022) 2402–2409.
[75] A.H. Cottrell and M.A. Jaswon: Distribution of solute atoms round a slow dislocation, Proc. R. Soc. Lond. A **199** (1949) 104–114.
[76] R. Fuentes-samaniego, R. Gasca-Neri and J.P. Hirth: Solute drag on

moving edge dislocations, Philos. Mag. A **49** (1984) 31–43.
[77] H. Yoshinaga and S. Morozumi: The solute atmosphere round a moving dislocation and its dragging stress, Philos. Mag. **23** (1971) 1367–1385.
[78] H. Yoshinaga and S. Morozumi: A Portevin-Le Chatelier effect expected from solute atmosphere dragging, Philos. Mag. **23** (1971) 1351–1366.
[79] R.B. Sills and W. Cai: Solute drag on perfect and extended dislocations, Philos. Mag. **96** (2016) 895–921.
[80] E.N. Epperly and R.B. Sills: Transient solute drag and strain aging of dislocations, Acta Mater. **193** (2020) 182–190.
[81] Y. Estrin and L.P. Kubin: Local strain hardening and nonuniformity of plastic deformation, Acta Metall. **34** (1986) 2455–2464.
[82] T.H. Alden: Theory of mobile dislocation density: Application to the deformation of 304 stainless steel, Metall. Trans. A **18** (1987) 51–62.
[83] T. Zirkle, L. Costello and D.L. McDowell: Crystal Plasticity Modeling of Hydrogen and Hydrogen-Related Defects in Initial Yield and Plastic Flow of Single-Crystal Stainless Steel 316L, Metall. Mater. Trans. A **52** (2021) 3961–3977.
[84] W.G. Johnston and J.J. Gilman: Dislocation velocities, dislocation densities, and plastic flow in lithium fluoride crystals, J. Appl. Phys. **30** (1959) 129–144.
[85] H. Saka: *Classical Theory of Crystal Dislocations: From Iron to Gallium Nitride*, (World Scientific Pub Co Inc, 2017).
[86] R. Horiuchi, H. Yoshinaga and S. Hama: New Yielding Phenomenon in Some Aluminium Alloys at High Temperatures, Trans. Japan Inst. Metals **6** (1965) 123–130.
[87] R. Horiuchi and H. Yoshinaga: Mechanism of the High Temperature Yield Point Phenomenon in Some Aluminium Alloys, Trans. Japan Inst. Metals **6** (1965) 131–138.
[88] G. Girardin, C. Huvier, D. Delafosse and X. Feaugas: Correlation between dislocation organization and slip bands: TEM and AFM investigations in hydrogen-containing nickel and nickel–chromium, Acta Mater. **91** (2015) 141–151.
[89] S. Wang, A. Nagao, K. Edalati, Z. Horita and I.M. Robertson: Influence of hydrogen on dislocation self-organization in Ni, Acta Mater. **135** (2017) 96–102.
[90] Q. Sun, J. He, A. Nagao, Y. Ni and S. Wang: Hydrogen-prompted heterogeneous development of dislocation structure in Ni, Acta Mater. **246** (2023) 118660.
[91] Y. Ogawa and A. Shibata: Plastic flow in Fe-Cr-Ni austenitic steel under the presence of solute H: A study via room temperature creep, Acta Mater. **285** (2025) 120659.
[92] U.F. Kocks, A.S. Argon and M.F. Ashby: Thermodynamics and Kinetics of Slip, Prog. Mater. Sci. **19** (1975) 1–291. https://linkinghub.elsevier.com/retrieve/pii/0079642575900055.
[93] J.L. Martin, B. Lo Piccolo, T. Kruml and J. Bonneville: Characterization of thermally activated dislocation mechanisms using transient tests, Mater. Sci. Eng. A **322** (2002) 118–125.
[94] P. Groh and R. Conte: Stress relaxation and creep in α-iron filamentary single crystals at low temperature, Acta Metall. **19** (1971) 895–902.
[95] P. Spätig, J. Bonneville and J.-L. Martin: A new method for activation volume measurements: application to Ni3(Al,Hf), Mater. Sci. Eng. A **167** (1993) 73–79.
[96] A.G. Evans and R.D. Rawlings: The Thermally Activated Deformation of Crystalline Materials, Phys. Status Solidi B **34** (1969) 9–31.
[97] U.F. Kocks: Superposition of Alloy Hardening, Strain Hardening, and Dynamic Recovery, in: *Strength of Metals and Alloys*, (Elsevier, 1979) pp. 1661–1680. https://doi.org/10.1016/B978-1-4832-8412-5.50250–2.
[98] R.A. Mulford: Analysis of strengthening mechanisms in alloys by means of thermal-activation theory, Acta Metall. **27** (1979) 1115–1124.
[99] P. Haasen: Plastic deformation of nickel single crystals at low temperatures, Philos. Mag. **3** (1958) 384–418.
[100] Y. Dong, T. Nogaret and W.A. Curtin: Scaling of Dislocation Strengthening by Multiple Obstacle Types, Metall. Mater. Trans. A **41** (2010) 1954–1960.
[101] W.A. Curtin: New interpretation of the Haasen plot for solute-strengthened alloys, Scr. Mater. **63** (2010) 917–920.
[102] S. Mishra, V.K. Beura, A. Singh and M. Yadava: Effect of obstacle strength and spacing on the slope of Haasen plot, Mater. Sci. Technol. **35** (2019) 403–408.
[103] S. Saimoto: The Characterization of Materials by Precision Strain Rate Sensitivity, J. Eng. Mater. Technol. **109** (1987) 230–235.
[104] S. Saimoto and B.J. Diak: Advanced method for structure-strength-ductility assessment of dispersion-strengthened FCC metals using activation work, mean slip distance and constitutive relation analyses: Decoding the Haasen plot, Mater. Sci. Eng. A **828** (2021) 142119.
[105] J.A. del Valle, A.C. Picasso and R. Romero: The superposition of flow stress contributions in a precipitate hardened Ni-based alloy studied by strain rate sensitivity measurements, Acta Mater. **51** (2003) 6443–6452.
[106] H. Mecking and U.F. Kocks: Kinetics of flow and strain-hardening, Acta Metall. **29** (1981) 1865–1875.
[107] A.H. Cottrell and R.J. Stokes: Effects of temperature on the plastic properties of aluminium crystals, Proc. R. Soc. Lond. A **233** (1955) 17–34.
[108] Z.S. Basinski, R.A. Foxall and R. Pascual: Stress equivalence of solution hardening, Scr. Metall. **6** (1972) 807–814.
[109] N.F. Mott and F.R.N. Nabarro: Dislocation theory and transient creep, in: *Physical Society Bristol Conference Report*, (1948) pp. 1–19.
[110] R.L. Fleischer: Substitutional solution hardening, Acta Metall. **11** (1963) 203–209.
[111] R.L. Fleischer: Solution hardening, Acta Metall. **9** (1961) 996–1000.
[112] R. Labusch: A Statistical Theory of Solid Solution Hardening, Phys. Status Solidi B **41** (1970) 659–669.
[113] J.C. Fisher: Application of Cottrell's theory of yielding to delayed yield in steel, Trans. ASM **47** (1955) 451–462.
[114] R. Kirchheim: Reducing grain boundary, dislocation line and vacancy formation energies by solute segregation. I. Theoretical background, Acta Mater. **55** (2007) 5129–5138.
[115] R. Kirchheim: Revisiting hydrogen embrittlement models and hydrogen-induced homogeneous nucleation of dislocations, Scr. Mater. **62** (2010) 67–70.
[116] J. Friedel: *Dislocations*, 1st ed., (Pergamon Press, 1964).
[117] A. Atrens, N.F. Fiore and K. Miura: Dislocation damping and hydrogen pinning in austenitic stainless steels, J. Appl. Phys. **48** (1977) 4247–4251.
[118] Y. Yagodzinskyy, M. Ivanchenko and H. Hänninen: Hydrogen-Dislocation Interaction in Austenitic Stainless Steel Studied with Mechanical Loss Spectroscopy, Solid State Phenomena **184** (2012) 227–232.
[119] R.A. Oriani: The diffusion and trapping of hydrogen in steel, Acta Metall. **18** (1970) 147–157.
[120] V.G. Gavriljuk and H. Berns: *High Nitrogen Steels Structure, Properties, Manufacture, Applications*, (Springer, 1999).
[121] Y. Dong and W.A. Curtin: Thermally activated plastic flow in the presence of multiple obstacle types, Model. Simul. Mater. Sci. Eng. **20** (2012) 075006.
[122] G. Schoeck: The superposition of thermal activation in dislocation movement, Phys. Status Solidi A **87** (1985) 571–581.